NBS TECHNICAL NOTE 1314

U.S. DEPARTMENT OF COMMERCE / National Bureau of Standards

Electromagnetic Fields Radiated From Electrostatic Discharges Theory and Experiment

Perry F. Wilson
Arthur R. Ondrejka
Mark T. Ma
John M. Ladbury

The National Bureau of Standards[1] was established by an act of Congress on March 3, 1901. The Bureau's overall goal is to strengthen and advance the nation's science and technology and facilitate their effective application for public benefit. To this end, the Bureau conducts research to assure international competitiveness and leadership of U.S. industry, science and technology. NBS work involves development and transfer of measurements, standards and related science and technology, in support of continually improving U.S. productivity, product quality and reliability, innovation and underlying science and engineering. The Bureau's technical work is performed by the National Measurement Laboratory, the National Engineering Laboratory, the Institute for Computer Sciences and Technology, and the Institute for Materials Science and Engineering.

The National Measurement Laboratory

Provides the national system of physical and chemical measurement; coordinates the system with measurement systems of other nations and furnishes essential services leading to accurate and uniform physical and chemical measurement throughout the Nation's scientific community, industry, and commerce; provides advisory and research services to other Government agencies; conducts physical and chemical research; develops, produces, and distributes Standard Reference Materials; provides calibration services; and manages the National Standard Reference Data System. The Laboratory consists of the following centers:

- Basic Standards[2]
- Radiation Research
- Chemical Physics
- Analytical Chemistry

The National Engineering Laboratory

Provides technology and technical services to the public and private sectors to address national needs and to solve national problems; conducts research in engineering and applied science in support of these efforts; builds and maintains competence in the necessary disciplines required to carry out this research and technical service; develops engineering data and measurement capabilities; provides engineering measurement traceability services; develops test methods and proposes engineering standards and code changes; develops and proposes new engineering practices; and develops and improves mechanisms to transfer results of its research to the ultimate user. The Laboratory consists of the following centers:

- Applied Mathematics
- Electronics and Electrical Engineering[2]
- Manufacturing Engineering
- Building Technology
- Fire Research
- Chemical Engineering[3]

The Institute for Computer Sciences and Technology

Conducts research and provides scientific and technical services to aid Federal agencies in the selection, acquisition, application, and use of computer technology to improve effectiveness and economy in Government operations in accordance with Public Law 89-306 (40 U.S.C. 759), relevant Executive Orders, and other directives; carries out this mission by managing the Federal Information Processing Standards Program, developing Federal ADP standards guidelines, and managing Federal participation in ADP voluntary standardization activities; provides scientific and technological advisory services and assistance to Federal agencies; and provides the technical foundation for computer-related policies of the Federal Government. The Institute consists of the following divisions:

- Information Systems Engineering
- Systems and Software Technology
- Computer Security
- Systems and Network Architecture
- Advanced Computer Systems

The Institute for Materials Science and Engineering

Conducts research and provides measurements, data, standards, reference materials, quantitative understanding and other technical information fundamental to the processing, structure, properties and performance of materials; addresses the scientific basis for new advanced materials technologies; plans research around cross-cutting scientific themes such as nondestructive evaluation and phase diagram development; oversees Bureau-wide technical programs in nuclear reactor radiation research and nondestructive evaluation; and broadly disseminates generic technical information resulting from its programs. The Institute consists of the following Divisions:

- Ceramics
- Fracture and Deformation[3]
- Polymers
- Metallurgy
- Reactor Radiation

[1]Headquarters and Laboratories at Gaithersburg, MD, unless otherwise noted; mailing address Gaithersburg, MD 20899.
[2]Some divisions within the center are located at Boulder, CO 80303.
[3]Located at Boulder, CO, with some elements at Gaithersburg, MD

Electromagnetic Fields Radiated From Electrostatic Discharges—Theory and Experiment

Perry F. Wilson*
Arthur R. Ondrejka
Mark T. Ma
John M. Ladbury

Electromagnetic Fields Division
Center for Electronics and Electrical Engineering
National Engineering Laboratory
National Bureau of Standards
Boulder, Colorado 80303-3328

*Presently with BBC, Baden-Dattwil, Switzerland

U.S. DEPARTMENT OF COMMERCE, C. William Verity, Secretary

NATIONAL BUREAU OF STANDARDS, Ernest Ambler, Director

Issued February 1988

National Bureau of Standards Technical Note 1314
Natl. Bur. Stand. (U.S.), Tech Note 1314, 72 pages (Feb. 1988)
CODEN:NBTNAE

U.S. GOVERNMENT PRINTING OFFICE
WASHINGTON: 1988

CONTENTS

List of Figures

ELECTROMAGNETIC FIELDS RADIATED FROM ELECTROSTATIC DISCHARGES THEORY AND EXPERIMENT

Perry F. Wilson*, Arthur R. Ondrejka, Mark T. Ma, and John M. Ladbury
Electromagnetic Fields Division
National Bureau of Standards
Boulder, Colorado 80303

The fields radiated by electrostatic discharges (ESD) are studied both theoretically and experimentally. The ESD spark is modeled theoretically as an electrically short, time dependent, linear dipole situated above an infinite ground plane. Experimentally, sparks of varying voltages are generated by a commerically available simulator and used to excite a number of targets including (1) the extended inner conductor of a coaxial cable mounted in a ground plane, (2) direct discharges to a ground plane, (3) indirect radiation from a large metal plate, (4) a metal chair over a ground plane, and (5) a metal trash can. Results show that relatively low-voltage sparks (2 - 4 kV) excite the strongest radiated fields. This suggests that the spark fields can pose a significant interference threat to electronic equipment into the gigahertz range.

Key words: electrostatic discharge; pulsed current; radiated electric field; radiated magnetic field; spectrum; time-domain technique.

*Presently with BBC, Baden-Dattwil, Switzerland.

1. INTRODUCTION

Electrostatic discharge, or ESD, is a common phenomenon with the potential to seriously upset electronic equipment. Currently, electronics manufacturers and users spend large sums for ESD prevention. As a result, ESD testing is now a widespread practice. Considerable effort has gone into the study of the ESD currents to develop current simulators for simplifying and standardizing ESD testing. However, the ESD-radiated fields have received significantly less attention, and only a few measurements have appeared in the literature [1]. This is primarily because fast field pulses are difficult to measure with available antennas. The recent development by the National Bureau of Standards (NBS) of broadband, linear-phase, time-domain antennas gives us the necessary measurement capability. This report examines theoretically and experimentally ESD-related fields and seeks to better quantify their interference threat.

As the name implies, ESD consists of two different phases. Electrostatic refers to the relatively slow buildup of a local voltage differential and the associated static electric field. Discharge denotes the rapid transfer of the resultant accumulated charge due to the breakdown of an intervening insulator, typically air. The basic ESD phases are [2]: (1) the corona-generated rf fields, (2) the pre-discharge effects, (3) the discharge current, (4) the discharge electric field, and (5) the discharge magnetic field. Each can affect sensitive electronic equipment. The corona, pre-discharge effects, and channel development are briefly discussed in Section 2. However, the main threat comes from the currents and fields that result from actual discharge.

The ESD fields problem will be considered analytically in Section 3 based on a simple dipole model. The spark is modeled as an electrically short, time-dependent, linear source (or dipole) situated above an infinite ground plane. In practice, discharges are usually to some metal object such as an equipment case or metal cart. If we allow the dipole to be situated close to the ground plane, then locally this should approximately reproduce ESD field behavior. This model allows us to examine the electric and magnetic near-field components, either on the ground plane surface which affects direct penetration into equipment shielding, or radiated away from the ground plane as in the case of interference to nearby electronics. The model is suitable for experimental confirmation and parametric studies.

Section 4 discusses the measurement system and the experimental data. The measurement of unknown pulsed currents and fields requires that the system be carefully calibrated with known pulses. The system response may then be deconvolved out of the measured data to yield the true measured pulses. The details of this procedure as well as the system limitations are presented in Section 4.1. The test results are covered in Section 4.2. The basic procedure is to excite a metal object with a spark and measure the radiated electric field. The objects excited are (1) the extended inner conductor of a coaxial cable mounted in a ground plane, (2) direct discharges to a ground plane, (3) indirect radiation from a large, vectical, metal plate, (4) a metal chair over a ground plane, and (5) a metal trash can. We find that it is the low-voltage (2 - 4 kV), fast rise-time (less than 1 ns) sparks which produce the highest radiated electric field. This result is also expected from the theory, which predicts dependence of the

far-field radiation on the derivative of the current waveform. These fields often exceed 100 V/m at a distance of 1.5 m from the discharge point and clearly pose an interference threat to nearby electronics. The coaxial target also allows us to measure the current waveform which is then used in the theoretical model described in Section 3 to predict the radiated fields (both electric and magnetic). The agreement between theory and experiment, for the electric field only, is quite good considering the idealized nature of the model. The magnetic fields are not measured due to the lack of a suitable broadband H-field antenna.

We conclude with summary of the results and suggestions for further research.

2. PRE-DISCHARGE EFFECTS AND DISCHARGE CURRENT

Objects accumulate charge either triboelectrically or inductively. Triboelectric charging is a mechanical process whereby relative surface motion transfers charge. An example is a person walking on a carpet. Charge transfer depends on the amount of contact, surface smoothness, air humidity, contact pressure, the triboelectric properties of the rubbing materials, and the rate of relative motion [3]. Precautionary measures to prevent excess charging are an important step in ESD prevention. These include anti-static carpet, anti-static mats, and control of humidity. Despite these measures, charged persons and carts are probably unavoidable.

The voltage to which a person or cart can be charged is highly dependent on their capacitance. Human capacitance can be modeled using cylinders and spheres. Based on this type of calculation, a typical figure for the lumped capacitance of an adult slightly above ground is 100 pF [4]. Common voltage figures quoted are 8-10 kV [5] for a charged person, with some authors claiming voltages as great as 30 kV. However, corona bleed-off likely keeps the upper bound more on the order of 25 kV. Persons typically do not feel sparks due to voltages less than 3 kV. Thus, many potentially upsetting ESD events go undetected.

Induction charging is the result of exposing an ungrounded object to an electrostatic field [3]. This often happens during the packaging and transportation of electronics. Handling, conveyor belts and other friction sources can cause a substantial charge buildup on a box or plastic package. The resulting local electrostatic field can affect solid-state logic through bit reversal, charge drainage, and dielectric burn through [6].

Under normal conditions, a gas such as air is a very effective insulator. Electrons are tightly bound and current conduction is difficult. Atoms are free to move about but are constrained by collisions. Collision rates and speeds are determined by the gas type, pressure, and temperature. Free electrons and positive ions may be present, but their numbers are usually very low and their motion will be random. Thus, on average, there is no transfer of charge. Applying an electrostatic field introduces a bias to the movement of charged particles. Electrons will now attempt to flow toward the anode while positive ions will flow toward the cathode. Electrons are lighter than the positive ions (at a ratio of 1:1800) and have smaller collision cross sections. Therefore, electrons contribute the bulk of the current. High-field levels can lead to the development of a very low

impedance channel within the gas resulting in a rapid charge transfer. The process, referred to as the electrical breakdown of gas, is complicated and its study has been an important research area for over a century.

ESD depends on the creation of free electrons and the formation of a conductive channel, as sequenced in figure 1, which is based on cloud chamber observations [7]. In (a) electrons released from the cathode collide to form additional electrons, in effect creating an avalanche in the direction of the anode. As the electron avalanche progresses it leaves behind positive ions, the space charge or corona cloud, which sets up a field perpendicular to the applied field. This tends to keep the avalanche in a well-defined channel (b). The conductive channel will continue to grow toward the anode due to the applied field and also toward the cathode due to the large trailing space charge (c). When the channel reaches both terminals (d) a conductive bridge is formed and a large current (spark) is possible. The discharge rapidly drains the available charge and when the current drops below some critical value, the conductive channel fails.

The pre-discharge current i_p may be estimated by [8]

$$i_p = VCv_p \qquad (1)$$

where V is the applied voltage, C is the leader capacitance (on the order of 5 pF/cm), and v_p is the velocity at which the leader propagates. The propagation velocity depends primarily on the applied voltage. For example, a value of 0.05 cm/ns at 35 kV is quoted by Rhoades [8]. However, leader velocities for arbitrary voltages are not well known. Using these numbers for a 1.0-cm gap, we see that the pre-discharge current would be 8.75 A, and last for about 20 ns. Typical breakdown voltages are significantly less. Thus, a level of 8.75 A for the pre-discharge current may be considered an upper bound. As will be seen in Section 4, a current building up over a 20 ns period is relatively slow compared to the actual discharge current and is not expected to radiate significant fields. Higher voltages mean larger spark gaps and consequently long time to form the conductive channel. The result is a longer current rise time for higher applied voltages. Because many ESD hazards are related to the rate of change of the discharge current, equipment will sometimes pass high voltage tests and fail at lower discharge voltages. This counter-intuitive effect has been noted frequently in the literature, but is not yet universally recognized.

The pre-discharge fields and currents may pose a threat to sensitive electronics. However, because the actual discharge currents and fields associated with them are significantly higher, the pre-discharge effects are largely ignored when analyzing ESD hazards.

The discharge current depends on the RLC characteristics of the charge source, the charging voltage, the rate of approach leading to the discharge, the electrode geometry, the conductive channel characteristics, and the RLC characteristics of the discharge victim. Given the wide ranges these variables can cover, it is difficult to construct a simple, general model of an ESD event. However, efforts are underway by the IEEE, the IEC, and

others to develop standard current shapes, targets, and test configurations in order to make ESD testing more repeatable and meaningful.

For long-term ESD testing it is far too difficult and variable for persons to repeatedly charge and discharge themselves. Thus, most ESD testing is done with simulators. This raises the problem of how to design an RLC circuit which realistically simulates human characteristics. Initial proposals, such as the current version of IEC Publication 801-2 [9], suggest a simple RC circuit as shown in figure 2. Values proposed by various organizations range from 60 to 300 pF for C and 10 to 10000 Ω for R [10]. However, this model ignores the inductance inherent to a human discharge and is too simple to yield realistic results.

Richman [10-11] has proposed a dual RLC circuit, as shown in figure 3. This model recognizes that the hand-forearm (L_H,R_H,C_H) and body (L_B,R_B,C_B) have very different discharge characteristics and therefore should not be lumped together. A further refinement is that proposed by Boxleitner [5]. He adds a finger capacitance which modifies the initial spike, discharge path impedances, and lumped impedances for the discharge victim, in addition to the arm and body impedances of the dual LRC circuit.

A computer simulation of a discharge based on the dual RLC circuit model in figure 3 is shown in figure 4. The hand-forearm contribution discharges quickly and contributes the fast rise-time initial spike. The body circuit generates the longer tail as the bulk of the stored charge is dissipated. In this particular example, the rise time is approximately 0.7 ns. If lower inductances (than 0.1 μH) were used, still faster rise times would result. A much faster rise time of the discharge current has also been observed by actual measurements when a simulator is approached to a testing object with a higher speed [12-14].

The measurement of current shapes is very dependent on the bandwidth of the oscilloscope used, as well as the characteristics of the victim [15]. Initial measurements often used fairly slow oscilloscopes (less than 100 MHz bandwidth) and the very fast rise times possible for low voltage sparks were not immediately recognized. Thus, the contribution due to the hand-forearm was overlooked and the single RLC circuits resulted. At present, it is recognized that oscilloscopes with bandwidths of at least 1 GHz are necessary to characterize current waveforms. A computer simulation by Richman [15] illustrating how oscilloscope bandwidth affects the measured current waveform is given in figure 5. Our measurement system has an effective bandwidth on the order of 1 GHz.

3. DIPOLE MODEL OF THE ESD-RADIATED FIELDS

The fields due to ESD currents can penetrate equipment directly or excite apertures, seams, vents, input-output cables, and the like, and couple to susceptible internal circuitry. Thus, the designer seeks to minimize this coupling at frequencies where problems are expected to occur. Reciprocity dictates that inefficient receivers will also be poor radiators. Therefore, equipment which can pass stringent ESD tests are usually within FCC-type specifications for radiated EMI limits as well.

3.1 Electric Field

Electric fields tend to excite high-impedance antennas and voltage-sensitive circuitry. Unwanted coupling can therefore be reduced by keeping the impedance of any potential receiving antenna low. This may enhance magnetic field pickup, so there are typically trade-offs. The basic rule is to keep lines short. Boxleitner [5] presents a detailed discussion on how to lay out circuit boards to minimize line-antenna problems.

Honda and Ogura have performed field measurements for various idealized ESD events [1]. They charged a pair of colinear conductive cylinders one suspended above the other and then drop the upper cylinder to bring them together and create a spark. An example of their data is shown in figure 6. They measure a fairly broadband spectrum which widens with increasing applied voltage up to about 10 kV and then begins to decrease as corona increasingly dissipates the energy before the main discharge. Their data indicate that most of the ESD energy is at frequencies below 2 GHz. However, ESD spectral distribution will depend on the current waveform, conductor geometry, measurement position etc., in addition to the charging voltage. Thus, although the data in figure 6 are likely representative, much work remains toward well characterizing ESD in the frequency domain.

We will model an ESD discharge by a dipole of length $d\ell$ above a perfect ground, as shown in figure 7. We impose a cylindrical coordinate system (ρ,ϕ,z) centered along the dipole (at $z = z'$) and its image. At 3 GHz, 1 cm is equal to $\lambda/10$; thus, at ESD frequencies like those shown in figure 6, the spark gap (which corresponds to the dipole current source at $z = z'$) will be electrically short and a dipole model is reasonable. The fields may be analyzed using time-dependent scalar and vector potentials. The details are left to Appendix A.

Although figure 7 shows the dipole above ground, actual ESD events take place very near the victim conductor. Thus, we will let the dipole approach the ground, that is, $z' \approx 0$. With this condition the electric field is found to be (see eq. A23)

$$\bar{E}(\bar{r},t) = \bar{a}_\rho d\ell \frac{\eta_0}{2\pi} \frac{\rho z}{R^2} \left\{\frac{3}{R^2} i + \frac{1}{cR} \frac{\partial i}{\partial t}\right\}$$

$$+ \bar{a}_z d\ell \frac{\eta_0}{2\pi} \left\{\left[\frac{3z^2}{R^2} - 1\right] \frac{1}{R^2} i + \left[\frac{z^2}{R^2} - 1\right] \frac{1}{cR} \frac{\partial i}{\partial t}\right\}, \qquad (2)$$

where R and $\bar{r}$ are defined in figure 7, and i is the current waveform as a function of time evaluated at t - R/c. If the current waveform is known, this expression can be used to examine the resultant electric field either at the ground plane, which represents direct penetration into susceptible equipment, or in some spatial direction as in the case of radiation to a nearby victim. There are two basic factors controlling the magnitude of E. First, geometry factors such as $1/(cR)$ and $1/(R^2)$, and second, the current shape, including its derivative $(i, \partial i/\partial t)$. For example, if we consider geometry as the dominant factor, then in the near field (very small R) E should behave according to

$$\bar{E}(\bar{r},t) \sim d\ell \frac{\eta_0}{2\pi} \left\{\bar{a}_\rho \frac{3\rho z}{R^2} + \bar{a}_z\left[\frac{3z^2}{R^2} - 1\right]\right\} \frac{1}{R^2} i \qquad \text{(near field).} \quad (3)$$

Equation (3) suggests that the near-field E is controlled by the current waveform directly. If the victim is sensitive to electric field peaks then the hand-forearm portion of the discharge is the most hazardous. If the victim is upset by prolonged exposure, then the full-body discharge or current tail will be the most contributing factor.

The far-field E (large R) is dominated by

$$\bar{E}(\bar{r},t) \sim d\ell \frac{\eta_0}{2\pi} \left\{\bar{a}_\rho \frac{\rho z}{R^2} + \bar{a}_z\left[\frac{z^2}{R^2} - 1\right]\right\} \frac{1}{cR} \frac{\partial i}{\partial t} \qquad \text{(far field).} \quad (4)$$

Thus, here it is the derivative of the current shape that contributes most. This suggests that for longer interference paths, such as indirect radiation to nearby susceptible equipment, low-voltage sparks with fast rise times may be the most damaging. However, if we again examine (2), we see that variations in the current time dependence could be more important than the geometry factors. In any case, exact results can be computed by including all the terms in (2) with a known analytical waveform i(t).

In reality, it seems unreasonable to expect that current waveforms can be written exactly in terms of simple analytical functions and substituted into the field expressions. Thus, some approximation will be necessary. A simple approach is to express a measured current waveform as a sequence of linear splines, as outlined in Appendix A (eqs. A25-A30). This approach is compatible with our measurement system since we acquire the current waveforms using a digitizing oscilloscope, and the data points may be used directly to generate the linear spline. This method should provide accurate results, although there are some minor difficulties such as discontinuities in the derivative of the current waveform. An alternative is to approximate a measured current waveform as a summation of damped exponentials (see eq. A-31). Because the current is basically due to the discharge of RLC circuits, this approach should prove reasonable. In fact, the approximated expression may be realizable by a combination of simple circuits of lumped parameters.

In addition to the time behavior of the electric field we may take the Fourier transform and determine its spectral behavior. This again requires

that we know the current waveform. Expressions based on our linear current and damped exponential approximations are developed in Appendix B. These may be used to identify the dominant frequency components excited by an ESD signature.

3.2 Magnetic Field

Magnetic fields can be a greater interference hazard than electric fields because they penetrate low-impedance shields more effectively. They also excite apertures and seams as do electric fields. They are best received by low-impedance antennas, especially circuit loops. Thus, avoiding loops poses a difficult design problem because loops are often difficult to recognize. Boxleitner [5] discusses methods for minimizing loop area by proper routing techniques.

The magnetic field due to ESD radiation may be analyzed as was the electric field. We find that (see eq. A23)

$$\bar{H}(\bar{r},t) = \bar{a}_\phi \, d\ell \, \frac{1}{2\pi} \frac{\rho}{R} \left\{ \frac{1}{R^2} \, i + \frac{1}{cR} \frac{\partial i}{\partial t} \right\}. \qquad (5)$$

In the near-field region, $\bar{H}$ should behave according to

$$\bar{H}(\bar{r},t) \sim \bar{a}_\phi \, d\ell \, \frac{1}{2\pi} \frac{\rho}{R} \frac{1}{R^2} \, i \qquad \text{(near field)}, \qquad (6)$$

while in the far field we find

$$\bar{H}(\bar{r},t) \sim \bar{a}_\phi \, d\ell \, \frac{\rho}{R} \frac{1}{cR} \frac{\partial i}{\partial t} \qquad \text{(far field)}. \qquad (7)$$

The near-field magnetic field depends directly on the ESD current shape as did the electric field. Thus, we would expect the highest fields to be associated with the highest current levels. The far-field magnetic field is dependent on the time derivative of the current, as was the case with the electric field. Therefore, the low-voltage, fast rise-time sparks cause the most interference to nearby equipment.

4. MEASURED ESD CURRENT AND ELECTRIC-FIELD WAVEFORMS

The measurement of ESD currents and the associated electric fields is a difficult task because of the very fast, broadband signals involved. The time-domain instrumentation must respond to these signals with minimal distortion and drift. The measurement system assembled here represents a best effort using equipment available.

4.1 Instrumentation

The experimental setup used to measure the ESD characteristics is shown in figure 8. It consists of three separate parts: the source, the target, and the measurement system.

The source was a commercially available ESD simulator indicated in fig. 8a and was made of lumped-constant circuit elements to simulate a human body charged to a preset voltage level. The source is capable of generating voltages from 100 V to 25 kV. It can be set to produce successive discrete sparks at a chosen time interval.

One of the important targets we used in the experiment was provided by the same manufacturer who supplied the ESD source. It consists of a brass ball 8 mm in diameter (see fig. 8a), which is connected to a ground plane through a parallel cluster of five low-value carbon resistors. It thus provides a low-resistance path between the source and ground and a method of determining the ESD spark current by measuring the voltage across the resistors, since this voltage is proportional to the current through the resistors. This voltage was measured through an extended center conductor of a coaxial cable which was connected to the ball target through a matching 50-Ω resistor. In fact, this is the only target with which we can measure the ESD current.

The field measurement system consists of a newly designed broadband, UHF (NBS 200-1), time-domain TEM horn antenna (see Appendix C) placed over a conductive ground plane, a digitizing oscilloscope, and a desktop computer. The digitizing oscilloscope has two inputs enabling us to measure the current and radiated electric field simultaneously, as indicated by two different colors. The system was calibrated by measuring the impulse response of the individual components (for example, pads, coaxial cable, connectors, oscilloscope) and then deconvolving out these component frequency responses to give the true current and field waveforms.

The antenna has a flat frequency response (± 3 dB) from 40 MHz to 1.2 GHz with minimum phase distortion, which makes it ideal for measuring the broadband signals in the time domain. The ground plane is an indoor facility which has a finite time window. This time window is estimated by the indirect scattering fields interfering with the direct signal between the source and the antenna. The shortest reflective path determines the width of the time window. The facility used to make these measurements has a direct path which is approximately three meters shorter than the smallest reflection path, thus allowing roughly a 10-ns window. It is therefore possible to measure the spectral content of fields at 100 MHz and greater.

The oscilloscope used in this experiment has a sample rate of 40 megasamples per second, which is not sufficient to capture the high-speed pulses generated by a single ESD spark. It was therefore necessary to average successive ESD events to utilize the available bandwidth of 1 GHz. The measurements were deemed repeatable enough to allow this averaging without compromising the integrity of the signals. Measurements of ESD current and electric field were also made with a microwave antenna (NBS 50-2), which is flat (± 6 dB) with even broader frequency coverage (than the UHF, NBS 200-1) from 50 MHz to 4.5 GHz and a digitizing oscilloscope with a bandwidth of 18 GHz in order to verify that there was a negligible spectral content at frequencies beyond the range of the oscilloscope and UHF antenna used in the original measurements. No discernable decrease in rise and fall times was observed. Therefore, no further experiments were performed with this system.

Basic functions of the desktop computer are for data acquisition, digital deconvolution, and digital filtering.

The most likely cause of error in the voltage (thus current) measurements (fig. 8a) is the assumption that the ball target consists of a pure resistance over the entire frequency range of interest up to 1 GHz. It is possible, however, that the carbon resistors are somewhat reactive for certain frequencies causing the target to act as a low-pass filter.

The most likely cause of error in the field measurements (fig. 8b) is the lack of isolation of the ESD spark. As a result, the antenna receives field compnents not only from the discharge to the ball target but also from the ESD simulator. In fact, slight changes in the simulator positioning caused drastic variations in the resulting measured electric field. For this reason, every attempt was made to shield the simulator from the measuring antenna by using absorbing material. With the absorbers in place, the measured fields did not change significantly when the simulator was repositioned. The discharge to the ball target was then the primary radiation source as desired.

4.2 Experimental Results

Experiments were performed for a number of different target configurations. The targets used were (1) the low-impedance ball mounted in a ground plane (fig. 8a), (2) direct sparking to the ground plane, (3) a vertical, square (0.91 m on a side), metal plate mounted above a ground plane, (4) a metal chair insulated from the ground plane, and (5) a metal waste basket. Targets (2) through (5) may simulate some practical office environment. The low-impedance ball target allows us to capture both the current waveform and the transient electric field simultaneously. In all other cases only the electric field was measured. We also recorded the relative humidity of the room, the spark gap, and the minimum voltage at which we were able to generate a spark by the simulator. Typically, the gap was adjusted to create a preselected level for the minimum firing voltage. Thus, we quote only the firing voltage in the data discussion. In our measurements, we use only a stationary gap because our main objective was to vertify the theoretical model outlined in Section 3. Approaching a simulator (ESD source) toward a testing object with a variety of faster speeds such as that which was studied recently [12-14] would have increased the leading edge slope (rise time) of the spark current, and accordingly, the radiated field. Thus, in this sense the experimental data presented in this report are considered conservative.

Seven voltage levels up to 12 kV (1, 2, 4, 6, 8, 10, and 12 kV) were set to excite the coaxial ball target. For higher voltages, the clean window time on our indoor ground plane is not sufficient to obtain meaningful fields data. The measurement arrangement is shown in figure 9. The antenna was located at a distance of 1.5 m from the target at an angle of 20° with respect to the ground plane. At this distance the antenna will be most likely in the far-field range (distance no less than $\lambda/2\pi$, where λ is the wavelength) of the ESD source for frequencies above 30 MHz. As mentioned before, the ESD simulator itself also radiated significantly. To reduce this effect, absorber was placed between the simulator and the antenna. The antenna was positioned to receive the vertical component of

the electric field. The horizontal component is expected to be small because both the spark and target are vertically oriented [it can also be seen from the first term in (2)]. Measurements of the horizontal electric field confirmed this.

The results are shown in figures 10 through 16. Each figure shows the measured current, the measured vertical electric field, and the predicted vertical electric field based on (2) and (A29). For the 1-kV discharge, the current reaches a peak amplitude of 7 A with a rise time of 700 ps. The measured vertical electric field reaches a peak of more than 50 V/m in about 350 ps (approximately half the rise time of the current pulse). As expected from (4), the electric field behaves very much as the derivative of the current waveform. The predicted (theory) vertical electric field is qualitatively similar to the measured data with two exceptions: first, the peak amplitude is not as high as measured and second, the measured undershoot is significantly greater. The first difference is not unexpected. In order to apply the theoretical model we need to know the length of the radiating dipole ($d\ell$). We simply took it to be the height of the ball-target above the ground plane. However, the target consists not of a single vertical conductor, but rather of an array of parallel resistors which act somewhat like an array of lossy vertical dipoles. Thus, it is not obvious how to specify an equivalent dipole length in this case. In addition, the tip of the simulator is a small loop which may itself be radiating and is also unaccounted for in the model. The second difference (undershoot) is more problematic. It could be an antenna response artifact but in that case the system deconvolution should take it out. It may also be that the target is acting somewhat as a low-pass (capacitive) filter due to the high-frequency response of the parallel resistors. The target response is not accounted for in the deconvolution. The reason that this suggests itself is the expected derivative behavior of the field response. The negative slope of the current waveform in figure 10 is not fast enough to cause the observed undershoot. If the target response is slowing the leading and trailing edges, then both the peak amplitude and the undershoot will be underestimated by our theoretical model, as we are seeing. A target with ideal, flatter frequency response should give better agreement between theory and experiment. Nonetheless, the theoretical model presented here does predict well the basic electric-field behavior. The magnetic field may also be computed by (A29) with the same approximated current based on the measured result. In particular, under the ideal far-field condition, the amplitude of the computed magnetic field in A/m differs approximately from the electric field by 120π. Because no broadband H-field sensor is available for measuring the magnetic field to compare with the theoretical result, only one computed magnetic field for the 4-kV case is presented in figure 18.

Figure 11 shows the results for a 2-kV spark. The current amplitude is on the order of 11 A while the measured peak electric field is approximately 75 V/m. Both are increased from the corresponding 1-kV values. Beyond that, the same basic comments apply. Increasing the discharge voltage to 4 kV, as shown in figure 12, furthers this trend (26 A for current peak and 160 V/m for electric field peak). The peak field is now quite high. We expect much higher fields nearer the spark as will be discussed later. Raising the discharge voltage to 6 kV now reverses the growth trend. The peak current has fallen to 21 A while the peak electric field is down

significantly to 60 V/m, as shown in figure 13. For the 8-kV spark shown in figure 14, the current amplitude remains about the same (approximately 24 A), but the rise time of the waveform continues to slow. This reduces the radiated electric field. Similar comments apply to figure 15 (the 10-kV discharge) and to figure 16 (the 12-kV discharge). For the latter case the peak electric field is down to just 20 V/m. Thus, the field interference threat appears to be associated primarily with lower-voltage sparks. Here, the 4-kV case appears to radiate most strongly. The reason for this was discussed in Section 2. As the spark gap increases and the discharge voltage becomes higher, the channel formation slows and the channel resistance increases. These tend to slow the discharge current. However, the discharge now contains more energy due to the increased potential.

As the rise time of current waveforms becomes slower when the discharge voltage is increasing, the theoretical predictions become better. In figures 15 and 16, the deconvolution process of these slower pulses has added some noise to the current measurements. This appears clearly in the theoretical curves, but qualitatively, the agreement between theory and measurement is good. This supports the supposition that it is the target response to very fast currents that is causing the disagreement at the lower discharge voltages.

We were not able to place our broadband receiving antenna closer to the ESD spark since the antenna calibration required that it be in the far-field zone. We can, however, use the model to predict the discharge near field according to (2) or (3). Figure 17 shows the vertical electric field for the 4-kV (worst case) spark of figure 12. The distances chosen were 1.5 m as before, plus 1 m, 50 cm, 20 cm, and 10 cm. The near-field to far-field transition frequencies for these distances are respectively 32, 48, 95, 239, and 477 MHz. Thus, at 1.5 m, most of the received spectra would be far field while at 10 cm, a good portion is in the near field. The electric field increases as the observation point is brought nearer until at 10 cm a peak amplitude of over 4 kV/m is encountered. The waveform shape also tends toward the current profile (rather than the time derivative of the current for the far-field case) as indicated by (3). The field levels at 10-cm, 20-cm, and 50-cm distances in figure 17 are strictly theoretical and need to be confirmed through measurements. But they suggest that the fields due to low-level discharge voltages can be extremely high in the vicinity of the spark.

The ESD electric-field spectrum for the 4-kV spark of figure 12 is shown in figure 19. The primary spectral components are below 1 GHz which is consistent with the findings of Honda and Ogura [1]. Above 3 GHz, the spectrum is down to the noise of the system deconvolution. We have also observed field pulses faster than the 4-kV case discussed here. They are difficult to capture and analyze because of limitations in our digitizing oscilloscope. But we expect that the spectral content of some sparks may be quite strong up to frequencies on the order of 5 GHz.

The preceding results were for discharges into a coaxial target which allowed us to capture both the current and the field. However, as discussed, the target may be filtering the current somewhat and it certainly represents an idealized victim. Figures 20 through 23 show measured data for the vertical electric field created by a spark to a ground plane at

discharge voltages of 1, 2, 4, and 6 kV respectively. The antenna was positioned as in the ball-target measurements. The trend is similar to that above; the peak field level grows from 80 V/m at 1 kV to 100 V/m at 2 kV and then begins to fall to 75 V/m at 4 kV and 45 V/m at 6 kV. The maximum peak is smaller than ball-target discharges. But in this case the radiating dipole is significantly shorter. The largest gap was 1.2 mm for the 6-kV case as compared to the 39-mm spark gap for the ball-target measurements. Referring to (2), we expect that reducing the dipole length $d\ell$ by an order of magnitude would reduce the fields by a similar amount if the current waveform remained the same. However, measured data suggest that the fields are actually higher for the 1 and 2-kV cases (figs. 20 and 21 vs. figs. 10 and 11) and slightly reduced for the 4 and 6-kV cases (figs. 22 and 23 vs. figs. 12 and 13). The ground plane is a true low-impedance target with a very fast response (as opposed to the coaxial ball target necessary for current measurements) and should not slow the current discharge. These observations again imply that the actual current waveforms may be far faster than we have been able to measure here with the ball target. Regardless, the field levels for these discharges are considerable.

Perhaps more realistic than coaxial targets or ground planes are sparks to large metal objects, such as might be encountered in a normal working environment. As an example, we consider the indirect radiation from a large, square, vertical, metallic plate (0.915 m per side) as shown in figure 24. The plate was excited by a discharge to the back side so that direct radiation from both the spark and the simulator are shielded from the antenna (again positioned 1.5 m away from the plate). A high-impedance strap from the plate to the ground plane was also used to bleed off the acuumulated static charge, but this should not contribute greatly to the radiated field. The measured data for 5 and 7-kV sparks are shown in figures 25 and 26. Rather than receiving a single pulse as in the previous cases, the plate tends to resonate after being excited by the spark. The fields are higher for the 5-kV spark, with the peak amplitude reaching 100 V/m. There is definitely some contamination of the data due to reflections from walls and other scatterers after the 10-ns clean window time has been exceeded. However, the contamination is not believed very significant due to the highly directive property of the antenna. At least, the peak value of 45 V/m at 14 ns is quite real. Even when the contamination is substantial, the case may represent a more realistic laboratory environment. The 7-kV spark plate radiation is not nearly as significant. Only the shadow-side radiation was tested here. A thorough study by including the antenna-side exictations, edge excitations, variations in plate size, and other excitaion voltages would be of future interest.

Figure 27 shows the measurement configuration for radiation from a metal chair above the ground plane. The chair was insulated from the ground plane by plastic tabs on its feet and was also provided a high-impedance path to bleed off the static charge as for the plate. The antenna remains at a distance of 1.5 m away from the spark point as before. The chair was excited by 3 and 6-kV sparks. The results are shown in figures 28 and 29. Like the plate, the chair tends to resonate. For the 3-kV spark excitation the field amplitude is quite substantial. Again, some of the data may be contaminated after the 10-ns clean time. However, the basic indication is that the indirect field radiation is significant and long lived. The 6-kV spark excites a weaker field.

The measurement for a metal trash can in direct contact with the ground plane is shown in figure 30. The antenna is also placed 1.5 m away from the spark point. The received vertical electric field due to a 4-kV spark is shown in figure 31. The initial spike within the system's clean time exceeds 100 V/m, again demonstrating the threat of indirect radiated fields.

5. CONCLUDING REMARKS AND DISCUSSIONS

We have theoretically modeled the radiation from electrostatic discharges by a simple elementary dipole above a ground plane. Radiated fields were found to be dependent on two factors: the magnitude of the transient current and its rise time. One factor may be more dominating than the other, depending on whether the observation point is in the near-field or far-field region of the ESD spark. When an analytical expression for the ESD spark current is known, the electric and magnetic fields radiated from the ESD can be computed exactly by the theoretical model. We also implemented an experimental system with a newly designed broadband antenna and a time-domain facility to measure both the current (for one case with a ball target) and radiated electric field waveforms produced by a stationary ESD simulator. We approximated the measured current waveform with an analytical expression, computed the corresponding electric and magnetic fields, and found that the theoretical electric field agreed well with the measured result. The electric fields due to ESD events could be quite high (although brief), which are certainly capable of upsetting a nearby equipment. The radiated magnetic field was not meausred because of non-existence of a broadband H-sensor.

If better experimental results are to be expected, several changes could be made to the system. The better ball target with a constant impedance over the entire frequency range of interest and having a low profile and minimum radiation could be used to yield a more accurate measured current. A better shield for the ESD simulator is also needed so that the source will not interfere with the measurements.

It would be interesting to perform field measurements at positions closer to the discharge to see if the transition from di/dt to i, in addition to the change in peak amplitude, may also be observed. More accurate measurements could be realized by using an outdoor ground screen to obtain a much larger time window, thereby including the low-frequency content of the radiated field.

Measurements of magnetic fields constitute another interesting research topic, particularly in view of the fact that most shields are ineffective against low-impedance fields. Until a broadband H-antenna becomes a reality, we can only rely on theoretical predictions and estimation derived from the measured electric fields.

6. ACKNOWLEDGMENTS

We would like to thank Peter Richman, President of KeyTek Instrument Corp., who inspired us to set up this modest study and convinced us that the results would benefit the computer industry. Mr. Richman also critically reviewed this manuscript. We would also like to express our appreciation to our Center Director, J. C. French, for his support and encouragement. The enthusiastic assistance by our technician, H. W. Medley, during the course of measurements is also acknowledged.

7. REFERENCES

[1] Honda, M.; Ogura, Y. Electrostatic spark discharges - three critical factors. Proc. EOS/ESD Symp., EOS-7, 149-154, 1985; Minneapolis, MN.

[2] Richman, P. ESD simulation - configuring a full-performance facility. IEEE Int. Symp. on EMC; 381-385, Aug. 1983; Crystal City, VA.

[3] Bhar, T. B. Electrostatic discharge failure mechanisms of semiconductor devices. ITEM, 276-282, 1986.

[4] Byrne, W. W. The meaning of electrostatic discharge (ESD) in relation to the human body characteristics and electronic equipment. IEEE Int. Symp. on EMC; 369-380, Aug. 1983; Washington, D. C.

[5] Boxleitner, W. Electrostatic discharge. Key Tronic Corp. Doc. No. 36-2464, 1986.

[6] Woods, M. H.; Gear, G. A new electrostatic discharge failure mode. IEEE Trans. Electron Devices, ED-26, 16-21; Jan. 1979.

[7] Penning, F. M. Electrical Discharges in Gases. New York, NY: McMillan Co.; 1957.

[8] Rhoades, W. T. Achieving ESD equipment protection with emission controls. IEEE Int. Symp. on EMC; 232-237, Aug. 1985; Wakefield, MA.

[9] IEC Pub 801-2: Electrostatic Discharge for Industrial Process Control.

[10] Richman, P; Tasker, A. ESD Testing: the interface between simulator and equipment under test. 6th Int. Electromagn. Compat. Symp. Rec.; 25-30, March 1985; Zurich, Switzerland.

[11] Richman, P. Classification of ESD hand/metal current waves versus approach speed, voltage, electrode geometry, and humidity. IEEE Int. Symp. on EMC; 451-460, Sept. 1986; San Diego, CA.

[12] Daout, B.; Ryser, H. Fast discharge mode in ESD-testing. 6th Symp. and Tech. Exhibition on EMC; 41-46, March, 1985; Zurich, Switzerland.

[13] Daout, B; Ryser, H.; Germond, A.; Zweiacker, P.; The correlation of rising slope and speed of approach in ESD tests. 7th Symp. and Tech. Exhibition on EMC; 461-466, March, 1987; Zurich, Switzerland.

[14] Daout, B; Ryser, H.; The reproducibility of the rising slope in ESD testing. IEEE Symp. on EMC; 467-474, Sept., 1986; San Diego, CA.

[15] Richman, P. Computer modeling the effects of oscilloscope bandwidth on ESD waveforms, including arc oscillations. IEEE Int. Symp. on EMC; 238-245, Aug. 1985; Wakefield, MA.

[16] Le Vine, D. M.; Meneghini, R. Electromagnetic fields radiated from a lightning return stroke: application of an exact solution to Maxwell's equations. J. Geophys. Res., 83, no. C5; 2377-2384, May 1978.

[17] Lawton, R. A.; Ondrejka, A. R. Antennas and the associated time domain range for the measurement of impulsive fields. NBS Tech Note 1008, Nov., 1978; Boulder, CO.

APPENDIX A: Time-Dependent Fields Due to a Dipole Source

The fields due to a time-dependent radiation source may be found from the potentials $\Phi(\bar{r},t)$ and $\bar{A}(\bar{r},t)$ which are given by

$$\Phi(\bar{r},t) = \frac{1}{4\pi\varepsilon_0} \int_{V'} \frac{\rho(\bar{r}',t-R/c)}{R} dv', \text{ and}$$

$$\bar{A}(\bar{r},t) = \frac{\mu_0}{4\pi} \int_{V'} \frac{\bar{J}(\bar{r}',t-R/c)}{R} dv'. \tag{A1}$$

where $\bar{r}$ is the observation point, $\bar{r}'$ is the source point, $R = |\bar{r} - \bar{r}'|$ is the separation between the two, ρ is the charge distribution, $\bar{J}$ is the current distribution, c is the speed of light, ε_0 is the free-space permittivity, and μ_0 is the free-space permeability. The fields are related to the potentials according to

$$\bar{E}(\bar{r},t) = -\nabla\Phi(\bar{r},t) - \frac{\partial}{\partial t}\bar{A}(\bar{r},t), \text{ and}$$

$$\bar{H}(\bar{r},t) = \frac{1}{\mu_0} \nabla\times\bar{A}(\bar{r},t). \tag{A2}$$

The potentials satisfy the condition

$$\nabla\cdot\bar{A}(\bar{r},t) + \frac{1}{c^2}\frac{\partial}{\partial t}\phi(\bar{r},t) = 0,$$

which implies that

$$\Phi(\bar{r},t) = -c^2 \int_0^t \nabla\cdot\bar{A}(\bar{r},t')dt'. \tag{A3}$$

Thus we need only solve for $\bar{A}(\bar{r},t)$.

Consider a time-dependent dipole source above a perfect ground as shown in figure 7. We impose a cylindrical coordinate system and note that the system is invariant in ϕ. The fields for $z \geq 0$ will be due to the dipole source and its image. The current distribution $\bar{J}$ reduces to an elemental line current i oriented along the z-axis, the volume integrals simply introduce the line length $d\ell$, and (A1) reduces to

$$\bar{A}(\bar{r},t) = \sum_{j=1}^{2} \bar{A}_j(\bar{r},t), \qquad \text{where} \tag{A4}$$

$$\bar{A}_j(\bar{r},t) = \bar{a}_z \, d\ell \, \frac{\mu_0}{4\pi} \frac{i(z',t-R_j/c)}{R_j} .$$

In (A4) j=1 represents the actual dipole and j=2 its image. We may now solve for $\Phi(\bar{r},t)$. We find that

$$\nabla\cdot\bar{A}(\bar{r},t) = d\ell \, \frac{\mu_0}{4\pi} \sum_{j=1}^{2} \frac{\partial}{\partial z} \left(\frac{i(z',t-R_j/c)}{R_j}\right). \tag{A5}$$

If we let $u = t - R_j/c$, and let the argument of i be implicit, then

$$\frac{\partial}{\partial z} \left(\frac{i}{R_j}\right) = R_j^{-2} \left\{R_j \frac{\partial i}{\partial u} \frac{\partial u}{\partial z} - i \frac{\partial R_j}{\partial z}\right\}. \tag{A6}$$

Note that

$$\frac{\partial i}{\partial u} = \frac{\partial i}{\partial t}, \text{ and}$$
$$\frac{\partial u}{\partial z} = -\frac{1}{c} \frac{\partial R_j}{\partial z}. \tag{A7}$$

Thus,

$$\frac{\partial}{\partial z} \left(\frac{i(z',t-R_j/c)}{R_j}\right) = - R_j^{-2} \frac{\partial R_j}{\partial z} \left\{i + \frac{R_j}{c} \frac{\partial i}{\partial t}\right\}, \tag{A8}$$

and

$$\nabla\cdot\bar{A}(\bar{r},t) = - d\ell \, \frac{\mu_0}{4\pi} \sum_{j=1}^{2} R_j^{-2} \frac{\partial R_j}{\partial z} \left\{i + \frac{R_j}{c} \frac{\partial i}{\partial t}\right\}. \tag{A9}$$

It follows that

$$\Phi(\bar{r},t) = d\ell \, \frac{c^2\mu_0}{4\pi} \sum_{j=1}^{2} R_j^{-2} \frac{\partial R_j}{\partial z} \int_0^t \left\{i + \frac{R_j}{c} \frac{\partial i}{\partial t'}\right\} dt'. \tag{A10}$$

We may now solve for the field components.

We will begin with $\bar{H}(\bar{r},t)$. Substituting (A4) into (A2) yields

$$\nabla\times\bar{A}(\bar{r},t) = d\ell \, \frac{\mu_0}{4\pi} \sum_{j=1}^{2} \nabla\times\left(\bar{a}_z \frac{i}{R_j}\right) = - \bar{a}_\phi d\ell \, \frac{\mu_0}{4\pi} \sum_{j=1}^{2} \frac{\partial}{\partial\rho}\left(\frac{i}{R_j}\right). \tag{A11}$$

The ρ-derivative is analogous to the z-derivative found above. Thus,

$$\nabla\times\bar{A}(\bar{r},t) = \bar{a}_\phi d\ell\, \frac{\mu_0}{4\pi} \sum_{j=1}^{2} R_j^{-2} \frac{\partial R_j}{\partial \rho} \left(i + \frac{R_j}{c} \frac{\partial i}{\partial t}\right). \tag{A12}$$

Thus we have

$$\bar{H}(\bar{r},t) = \bar{a}_\phi d\ell\, \frac{1}{4\pi} \sum_{j=1}^{2} R_j^{-2} \frac{\rho}{R_j} \left(i + \frac{R_j}{c} \frac{\partial i}{\partial t}\right). \tag{A13}$$

In order to find $\bar{E}(\bar{r},t)$ we need to evaluate $\nabla\Phi$, where

$$\nabla\Phi(\bar{r},t) = \bar{a}_\rho \frac{\partial}{\partial\rho}\Phi(\bar{r},t) + \bar{a}_z \frac{\partial}{\partial z}\Phi(\bar{r},t). \tag{A14}$$

Taking the proper derivatives yields

$$\begin{aligned}
\frac{\partial}{\partial\rho}\left\{R_j^{-2} \frac{\partial R_j}{\partial z} \int_0^t \left(i + \frac{R_j}{c} \frac{\partial i}{\partial t'}\right)dt'\right\} &= \frac{-\rho(z\mp z')}{R_j^2}\left\{\frac{3}{R_j^3}\int_0^t i\,dt' + \frac{3}{cR_j^2} i + \frac{1}{c^2 R_j}\frac{\partial i}{\partial t}\right\}, \\
\frac{\partial}{\partial z}\left\{R_j^{-2} \frac{\partial R_j}{\partial z} \int_0^t \left(i + \frac{R_j}{c} \frac{\partial i}{\partial t'}\right)dt'\right\} &= \frac{1}{R_j^3}\left[1 - \frac{3(z\mp z')^2}{R_j^2}\right]\int_0^t i\,dt' \\
&\quad + \frac{1}{cR_j^2}\left[1 - \frac{3(z\mp z')^2}{R_j^2}\right] i - \frac{1}{c^2 R_j}\frac{(z\mp z')^2}{R_j^2}\frac{\partial i}{\partial t},
\end{aligned} \tag{A15}$$

where $\mp$ designates the source (-) and its image (+). Thus we find that (note that $c^2\mu_0 = 1/\varepsilon_0$)

$$\begin{aligned}
\nabla\Phi(\bar{r},t) = &- \bar{a}_\rho \frac{d\ell}{4\pi\varepsilon_0} \sum_{j=1}^{2} \frac{\rho(z\mp z')}{R_j^2}\left\{\frac{3}{R_j^3} I + \frac{3}{cR_j^2} i + \frac{1}{c^2 R_j}\frac{\partial i}{\partial t}\right\} \\
&+ \bar{a}_z \frac{d\ell}{4\pi\varepsilon_0} \sum_{j=1}^{2} \left\{\frac{1}{R_j^3}\left[1 - \frac{3(z\mp z')^2}{R_j^2}\right] I + \frac{1}{cR_j^2}\left[1 - \frac{3(z\mp z')^2}{R_j^2}\right] i - \frac{1}{c^2 R_j}\frac{(z\mp z')^2}{R_j^2}\frac{\partial i}{\partial t}\right\},
\end{aligned} \tag{A16}$$

where

$$I = I(z', t - R_j/c) = \int_0^t i(t' - R_j/c)\,dt'.$$

Next we calculate

$$\frac{\partial\bar{A}(\bar{r},t)}{\partial t} = \bar{a}_z\, d\ell\, \frac{\mu_0}{4\pi} \sum_{j=1}^{2} \frac{1}{R_j} \frac{\partial i}{\partial t} = \bar{a}_z\, d\ell\, \frac{1}{4\pi\varepsilon_0} \sum_{j=1}^{2} \frac{1}{c^2 R_j} \frac{\partial i}{\partial t}. \tag{A17}$$

Combining results we find that

$$\bar{E}(\bar{r},t) = \bar{a}_\rho \frac{d\ell}{4\pi\varepsilon_0} \sum_{j=1}^{2} \{\frac{\rho}{R_j} \frac{(\bar{z}+\bar{z}')}{R_j} [\frac{3}{R_j^3} I + \frac{3}{cR_j^2} i + \frac{1}{c^2 R_j} \frac{\partial i}{\partial t}]\}$$

$$+ \bar{a}_z \frac{d\ell}{4\pi\varepsilon_0} \sum_{j=1}^{2} \{[\frac{3(\bar{z}+\bar{z})^2}{R_j^2} - 1](\frac{1}{R_j^3} I + \frac{1}{cR_j^2} i) + [\frac{(\bar{z}+\bar{z}')^2}{R_j^2} - 1]\frac{1}{c^2 R_j} \frac{\partial i}{\partial t}\}. \quad (A18)$$

For a discharge to a conductor the spark will occur very close to the conductor surface, that is $z' \approx 0^+$. If we impose this condition we find that $R_j = R = (z^2 + \rho^2)^{1/2}$ and that

$$\bar{E}(\bar{r},t) = \bar{a}_\rho \frac{d\ell}{2\pi\varepsilon_0} \frac{\rho z}{R^2} \{\frac{3}{R^3} I + \frac{3}{cR^2} i + \frac{1}{c^2 R} \frac{\partial i}{\partial t}\}$$

$$+ \bar{a}_z \frac{d\ell}{2\pi\varepsilon_0} \{[\frac{3z^2}{R^2} - 1](\frac{1}{R^3} I + \frac{1}{cR^2} i) + [\frac{z^2}{R^2} - 1]\frac{1}{c^2 R} \frac{\partial i}{\partial t}\}, \text{ and}$$

$$\bar{H}(\bar{r},t) = \bar{a}_\phi \frac{d\ell}{2\pi} \frac{\rho}{R} \{\frac{1}{R^2} i + \frac{1}{cR} \frac{\partial i}{\partial t}\}. \quad (A19)$$

As a check note that in the far field the 1/R terms should dominate. If we convert to spherical coordinates we find that

$$\bar{E}(\bar{r},t) \sim \bar{a}_\theta \frac{d\ell}{2\pi\varepsilon_0} \frac{\sin\theta}{c^2 R} \frac{\partial i}{\partial t}, \text{ and}$$

$$\bar{H}(\bar{r},t) \sim \bar{a}_\phi \frac{d\ell}{2\pi} \frac{\sin\theta}{cR} \frac{\partial i}{\partial t}. \quad (A20)$$

Thus the wave impedance tends toward η_0 as expected.

Although, the above expressions have the correct radiation behavior, there is difficulty with this model in the very near field. Consider a static electric dipole $\bar{P}$ of length $d\ell$ along the z-axis,

$$\bar{P} = \bar{a}_z d\ell Q, \quad (A21)$$

where Q is the total charge on either pole. Note that Q is a measure of the net current either leaving or entering the pole,

$$Q = \pm \int_0^t i(t')dt', \quad (A22)$$

± depending on which pole is being considered. Thus, Q is related to I. The appearance of a $1/R^3$, static electric-dipole moment contribution is a result of the assumption that the dipole is short ($d\ell/R << 1$, $k_0(d\ell)^2/R << 1$). If instead we had considered a linear antenna with appreciable length and assumed the current to be a travelling wave, then the static I-dependent dipole moment term does not arise [16]. Although a dipole in free space can hold a static charge, our ESD system will not. The charge will actually decay rapidly due to the relatively low relaxation time ε/σ on a good conductor. Thus, we will neglect the I terms in our model. The field expressions therefore reduce to

$$\bar{E}(\bar{r},t) = \bar{a}_\rho \, d\ell \, \frac{\eta_0}{2\pi} \frac{\rho z}{R^2} \left\{\frac{3}{R^2} i + \frac{1}{cR} \frac{\partial i}{\partial t}\right\}$$

$$+ \bar{a}_z \, d\ell \, \frac{\eta_0}{2\pi} \left\{\left[\frac{3z^2}{R^2} - 1\right] \frac{1}{R^2} i + \left[\frac{z^2}{R^2} - 1\right] \frac{1}{cR} \frac{\partial i}{\partial t}\right\}, \text{ and} \qquad \text{(A23)}$$

$$\bar{H}(\bar{r},t) = \bar{a}_\phi \, d\ell \, \frac{1}{2\pi} \frac{\rho}{R} \left\{\frac{1}{R^2} i + \frac{1}{cR} \frac{\partial i}{\partial t}\right\}.$$

Equation (A23) allows us to consider the fields due to a short dipole near a ground plane. We wish to model either direct field penetration into the victim in which case $z = 0$, or the effect of radiated fields on nearby objects, for example due to a discharge to a metal cart. For the $z = 0$ case (direct victim penetration), $R = \rho$, $\bar{r}$ depends only on ρ,

$$\bar{E}(\rho,t) = - \bar{a}_z \, d\ell \, \frac{\eta_0}{2\pi} \left\{\frac{1}{\rho^2} i + \frac{1}{c\rho} \frac{\partial i}{\partial t}\right\}, \text{ and}$$

$$\bar{H}(\bar{r},t) = \bar{a}_\phi \, d\ell \, \frac{1}{2\pi} \left\{\frac{1}{\rho^2} i + \frac{1}{c\rho} \frac{\partial i}{\partial t}\right\}. \qquad \text{(A24)}$$

Thus, on the ground screen in the transitional near field, not too close to the dipole as per our assumptions, the wave impedance retains the far-field value of 120π Ω.

In general the time behavior of an actual ESD current will be quite erratic; thus, we do not expect to be able to model it by a simple analytic function. One approach is to approximate the current by a series of linear functions, each valid over a small interval. By choosing the number of intervals to be large we should be able to generate an accurate model. In particular, we will use a set of ramp functions

$$i(0^+,t) = \sum_{n=0}^{N} i_n(t), \qquad \text{(A25)}$$

where

$$i_n(t) = 0 \qquad \text{for } t \leq t_n,$$

$$i_n(t) = a_n \frac{\Delta t_n}{\Delta_n} \qquad \text{for } t_n \leqq t \leqq t_{n+1}, \text{ and} \tag{A26}$$

$$i_n(t) = a_n \qquad \text{for } t_{n+1} \leqq t.$$

where $\Delta t_n = t - t_n$, and $\Delta_n = t_{n+1} - t_n$. With this linear approximation we see that

$$\frac{\partial}{\partial t} i(0^+, t-R/c) = \sum_{n=0}^{N} \frac{\partial}{\partial t} i_n(t-R/c). \tag{A27}$$

Evaluating (A23) yields

$$\frac{\partial}{\partial t} i_n = 0 \qquad \text{for } t-R/c \leqq t_n,$$

$$\frac{\partial}{\partial t} i_n = \frac{a_n}{\Delta_n} \qquad \text{for } t_n \leqq t-R/c \leqq t_{n+1}, \text{ and} \tag{A28}$$

$$\frac{\partial}{\partial t} i_n = 0 \qquad \text{for } t_{n+1} \leqq t-R/c.$$

Thus, for this approximation we have a discontinuous derivative. If we substitute these into the field expressions (A23) we find the following approximate forms

$$\bar{E}(\bar{r},t) = d\ell \frac{\eta_0}{2\pi} \left\{ \bar{a}_\rho \frac{\rho z}{R^2} \sum_{n=0}^{N} E_{\rho n} + \bar{a}_z \sum_{n=0}^{N} E_{zn} \right\}, \text{ and} \tag{A29}$$

$$\bar{H}(\bar{r},t) = \bar{a}_\phi \frac{d\ell}{2\pi} \frac{\rho}{R} \sum_{n=0}^{N} H_{\phi n},$$

where

$$E_{\rho n} = 0 \qquad \text{for } t - R/C \leqq t_n,$$

$$E_{\rho n} = \frac{a_n}{\Delta_n} \frac{1}{R^2} \left\{ 3\Delta t_n + \frac{R}{c} \right\} \qquad \text{for } t_n < t-R/c \leqq t_{n+1},$$

$$E_{\rho n} = a_n \frac{3}{R^2} \qquad \text{for } t_{n+1} < t-R/c,$$

$$E_{zn} = 0 \qquad \text{for } t-R/c < t_n, \tag{A30}$$

$$E_{zn} = \frac{a_n}{\Delta_n} \frac{1}{R^2} \left\{ \left(\frac{3z^2}{R^2} - 1\right)\Delta t_n + \left(\frac{z^2}{R^2} - 1\right)\frac{R}{c} \right\} \qquad \text{for } t_n < t-R/c \leqq t_{n+1},$$

$$E_{zn} = a_n \frac{1}{R^2} \left(\frac{3z^2}{R^2} - 1\right), \qquad \text{for } t_{n+1} < t-R/C,$$

$$H_{\phi n} = 0 \qquad \text{for } t-R/c \leqq t_n,$$

$$H_{\phi n} = \frac{a_n}{\Delta_n}\left\{\frac{1}{R^2}\,\Delta t_n + \frac{1}{cR}\right\} \qquad \text{for } t_n < t-R/c \le t_{n+1}, \text{ and}$$

$$H_{\phi n} = a_n \frac{1}{R^2} \qquad \text{for } t_{n+1} < t-R/c.$$

These may be readily found via computer once a linear spline approximation to a current waveform is given.

An alternative to a direct point-matching approach such as outlined above, is to fit a sequence of damped exponentials to the current waveform based on Prony's method. Let

$$i(t) = \sum_{n=1}^{N} a_n e^{-b_n t} \tag{A31}$$

for $t \ge 0$ and $i(t) = 0$ for $t<0$. Continuity thus implies that the summation of the a_n be zero. The derivatives of this form are readily found and the result will be continuous. The derivative will not be continuous at $t = 0$ unless further conditions are imposed. Inserting the exponential fit (A31) into the field expressions (A23) yields

$$\bar{E}(\bar{r},t) = \bar{a}_\rho \, d\ell \, \frac{\eta_0}{2\pi} \frac{\rho z}{R^2} \sum_{n=1}^{N} a_n e^{-b_n t} \left\{\frac{3}{R^2} - \frac{1}{cR}\, b_n\right\}$$

$$+ \bar{a}_z \, d\ell \, \frac{\eta_0}{2\pi} \sum_{n=1}^{N} a_n e^{-b_n t} \left\{\left[\frac{3z^2}{R^2} - 1\right]\frac{1}{R^2} - \left[\frac{z^2}{R^2} - 1\right]\frac{1}{cR}\, b_n\right\}, \text{ and} \tag{A32}$$

$$\bar{H}(\bar{r},t) = \bar{a}_\phi \, d\ell \, \frac{1}{2\pi} \frac{\rho}{R} \sum_{n=1}^{N} a_n e^{-b_n t} \left\{\frac{1}{R^2} - \frac{1}{cR}\, b_n\right\}.$$

APPENDIX B: Spectrum of ESD Dipole Radiation Model

If the field components are determined in the time domain, the spectrum may be found by taking the Fourier transform according to

$$\bar{F}(\bar{r},\omega) = \int_{-\infty}^{\infty} \bar{F}(\bar{r},t)e^{-j\omega t}dt, \tag{B1}$$

where $\bar{F}$ represents one of the fields. Substituting in the field expressions for $\bar{E}$ and $\bar{H}$ (eq. A23) leads to two integrals that need to be evaluated:

$$\int_{-\infty}^{\infty} i(t)\, e^{-j\omega t}dt, \qquad \text{and}$$

$$\int_{-\infty}^{\infty} \frac{\partial i(t)}{\partial t}\, e^{-j\omega t}dt. \tag{B2}$$

If the second integral is integrated by parts we find that

$$\int_{-\infty}^{\infty} \frac{\partial i(t)}{\partial t}\, e^{-j\omega t}dt = i(t)e^{-j\omega t}\Big|_{-\infty}^{+\infty} + j\omega \int_{-\infty}^{\infty} i(t)\, e^{-j\omega t}dt. \tag{B3}$$

For a pulse of finite duration, $i(t) = 0$ at both the endpoints and (B3) reduces to

$$\int_{-\infty}^{\infty} \frac{\partial i(t)}{\partial t}\, e^{-j\omega t}dt = j\omega \int_{-\infty}^{\infty} i(t)e^{-j\omega t}dt. \tag{B4}$$

Thus, we need only consider this single integral in order to evaluate (B1).

We will again represent the current by a sum of linear functions (A25) as detailed in Appendix A. The pulse is zero outside the interval $t \in (0, t_{N+1})$ where we will evaluate the integral in terms of retarded time ($t-R/c \rightarrow t$). Thus we have

$$\begin{aligned}\int_0^{t_{N+1}} i(t)\, e^{-j\omega t}dt &= \sum_{n=0}^{N} \int_0^{t_{N+1}} i_n(t)\, e^{-j\omega t}dt \\ &= \sum_{n=0}^{N} \left\{\frac{a_n}{\Delta_n} \int_{t_n}^{t_{n+1}} (t-t_n)\, e^{-j\omega t}dt + a_n \int_{t_n}^{t_{N+1}} e^{-j\omega t}dt\right\}.\end{aligned} \tag{B5}$$

Evaluating the various integrals and combining results yields

$$\int_0^{t_{N+1}} i(t)\, e^{-j\omega t}\, dt = \sum_{n=0}^{N} \frac{a_n}{\Delta_n} \frac{e^{-j\omega t_n}}{\omega^2} \{e^{-j\omega\Delta_n} - 1\} + j \frac{e^{-j\omega t_{N+1}}}{\omega} \sum_{n=0}^{N} a_n. \tag{B6}$$

For a pulse of finite duration, the a_n summation is zero. For convenience, let $S(\omega)$ denote the remaining summation in (B6); that is

$$S(\omega) = \sum_{n=0}^{N} \frac{a_n}{\Delta_n} \frac{e^{-j\omega t_n}}{\omega^2} \{e^{-j\omega\Delta_n} - 1\}. \tag{B7}$$

The field component spectra are found to be

$$\bar{E}(\bar{r},\omega) = \bar{a}_\rho\, d\ell\, \frac{\eta_0}{2\pi} \frac{\rho z}{R^2} \{\frac{3}{R^2} + \frac{j\omega}{cR}\} S(\omega)$$

$$+ \bar{a}_z\, d\ell\, \frac{\eta_0}{2\pi} \{(\frac{3z^2}{R^2} - 1)\frac{1}{R^2} + (\frac{z^2}{R^2} - 1)\frac{j\omega}{cR}\} S(\omega), \text{ and} \tag{B8}$$

$$\bar{H}(\bar{r},\omega) = \bar{a}_\phi\, \frac{d\ell}{2\pi} \frac{\rho}{R} \{\frac{1}{R^2} + \frac{j\omega}{cR}\} S(\omega).$$

We may also consider the damped exponential form for the current given by (A31). In this case the equivalent expression to (B5) is

$$\int_{-\infty}^{\infty} i(t)\, e^{-j\omega t}\, dt = \sum_{n=0}^{N} a_n \int_0^{\infty} e^{-(b_n + j\omega)t}\, dt$$

$$= \sum_{n=0}^{N} a_n \frac{1}{b_n + j\omega} = T(\omega). \tag{B9}$$

The spectra of the $\bar{E}$ and $\bar{H}$ fields will be again given by (B8) with $T(\omega)$ substituted for $S(\omega)$.

APPENDIX C: Time-Domain Antennas for Measuring Impulsive Electromagnetic Fields

Since the purpose of our experiment was to study the temporal characteristics of the electromagnetic fields emitted from ESD events, it was important to choose a broadband receiving antenna that had the greatest possible fidelity. Some antennas produced severe distortion in the time-domain waveform because of their poor phase response even though they did have flat characteristics in the frequency domain. The antenna used for the major part of the work is called UHF antenna (NBS 200-1), which is basically a truncated TEM horn as shown in figure 32. Two elements of this antenna form a parallel-plate transmission line, whose impedance depends on the ratio of the distance between the elements to their width. Since this ratio is constant, the antenna impedance remains 200 Ω within its designed operating frequency range (from 40 MHz to 1.2 GHz). At the antenna feed point, there is a pulse transformer, which terminates, on one side, the elements in 200 Ω and produces a 50 Ω output on the other side. The details of this pulse transformer are given in figure 33. It is this pulse transformer which maintains the correct impedance up to 1.2 GHz. Consequently, the standing waves of the antenna are negligibly small, and the frequency response is flat within ± 3 dB in the designed frequency range of 40 MHz to 1.2 GHz with usable response even down to 20 MHz, as shown in figure 34. The time-domain response of this antenna to the transmitting pulse shown in figure 35 is presented in figure 36. This antenna has a risetime response of about 300 ps.

Another modified version called the microwave antenna (NBS 50-2) also has excellent fidelity and flat frequency response with a broader designed operating frequncy range (from 50 MHz to 4.5 GHz). The antenna elements are designed to have an impedance of only 100 Ω, each element of the antenna being 50 Ω with respect to a ground plane located in the middle of the antenna, as shown in figure 37. Each element is brought out on a separate coaxial line. The previously used pulse transformer is now replaced with a broadband balun (see fig. 38). The balun accepts two input signals which are 180 degrees out of phase with each other and combines them in a broadband resistive power combiner (splitter in the figure) providing a single 50 Ω output. Details of this antenna are available in [17]. This antenna was used only for that part of the experiment where we were searching potential spectra which may fall outside of the UHF antenna frequency range, as mentioned in Section. 4.1.

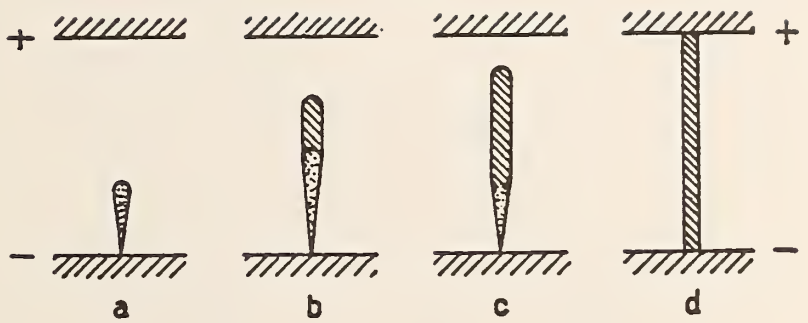

Figure 1. Diagrams showing the development of a spark channel, based on cloud chamber observations: (a) electron avalanche, (b) channel growth toward anode , (c) channel growth toward both anode and cathode, and (d) conductive bridge [7].

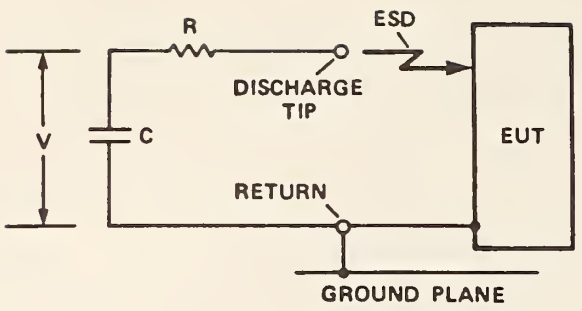

Figure 2. Conventional single RC circuit model for human electrostatic discharge [9].

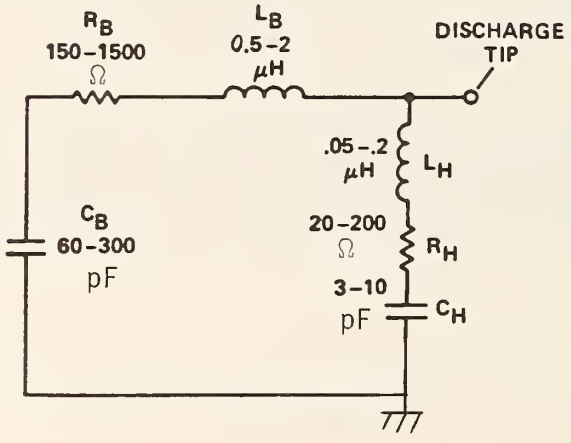

Figure 3. The dual RLC circuit model for human electrostatic discharge incorporating separate, parallel paths for body and hand discharges [11].

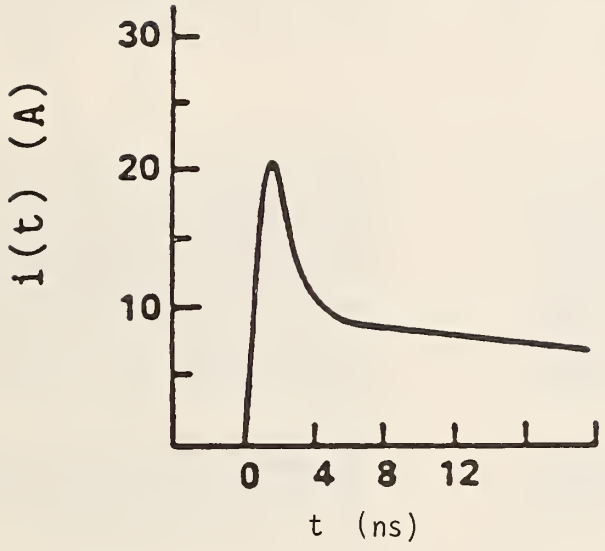

Figure 4. Computer simulation of an ESD current based on the dual RLC circuit (fig. 3). The circuit parameters used are C_H=7.5 pF, R_H=200 Ω, L_H=0.1 μH, C_B=100 pF, R_B=500 Ω, L_B=1.7 μH, and 5-kV initial charge [11].

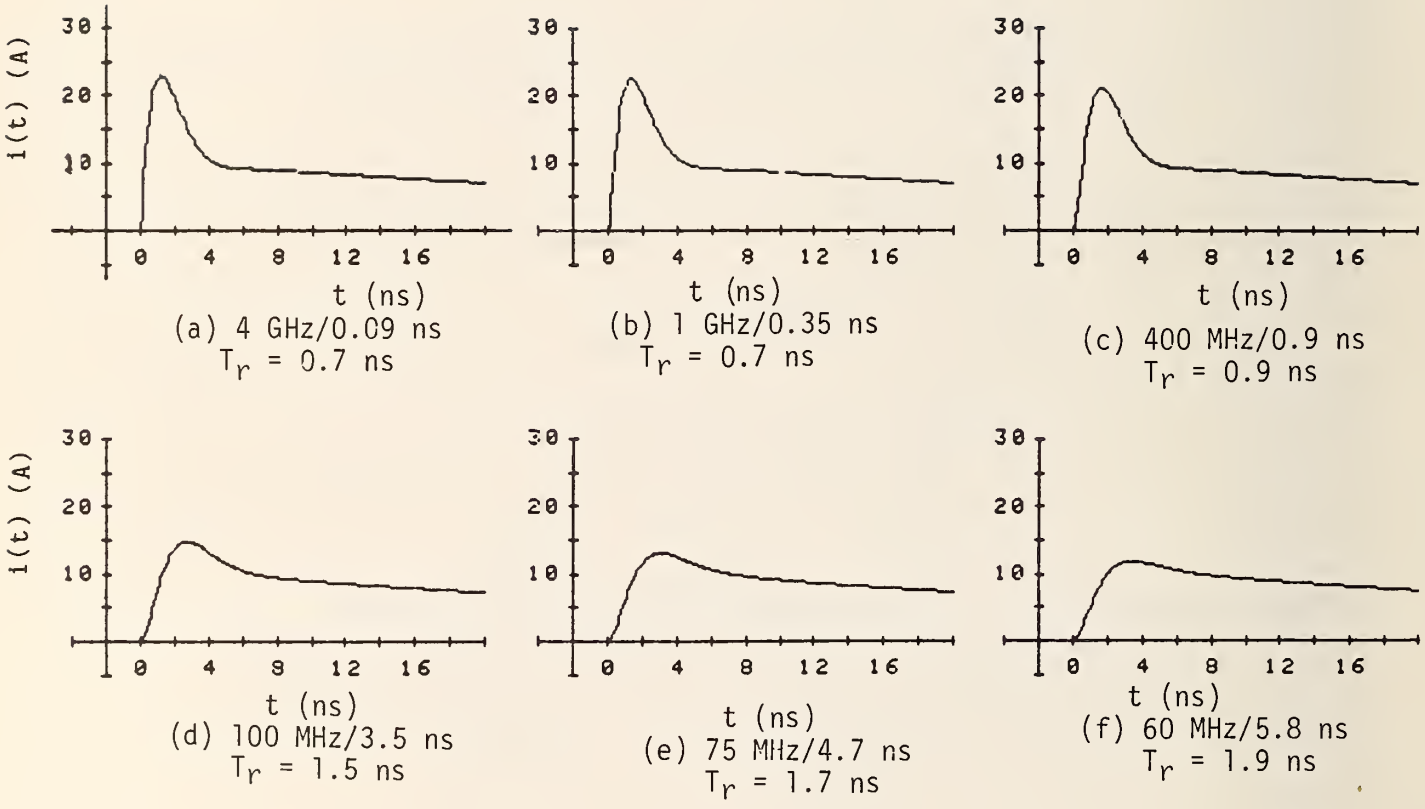

Figure 5. Computer solutions for a dual RLC-circuit model using different single-pole simulated oscilloscope bandwidths. The initial applied voltage is 5 kV [15].

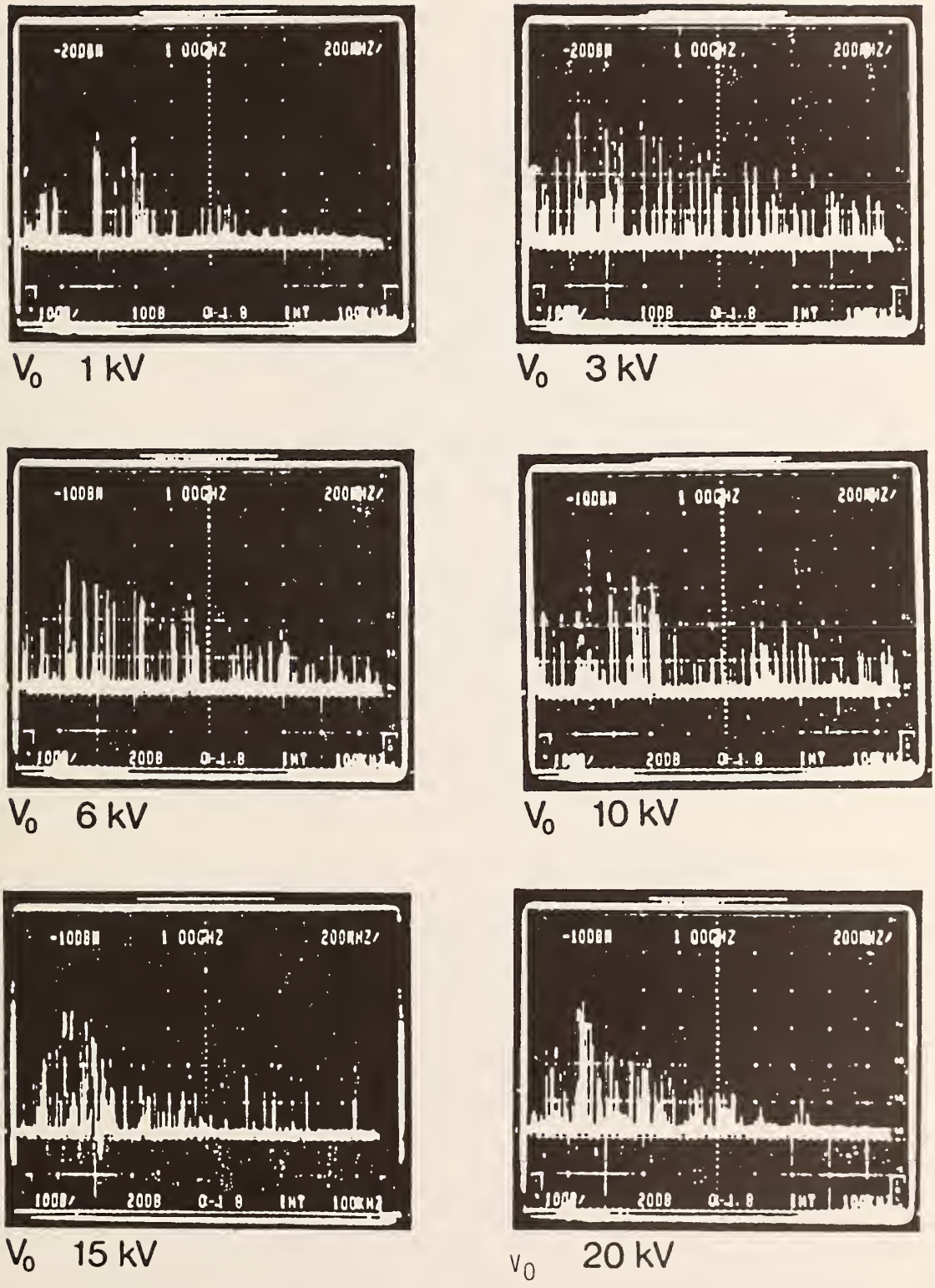

Figure 6. The radiation spectrum at 2.0 m from an ESD source for various applied voltages [1].

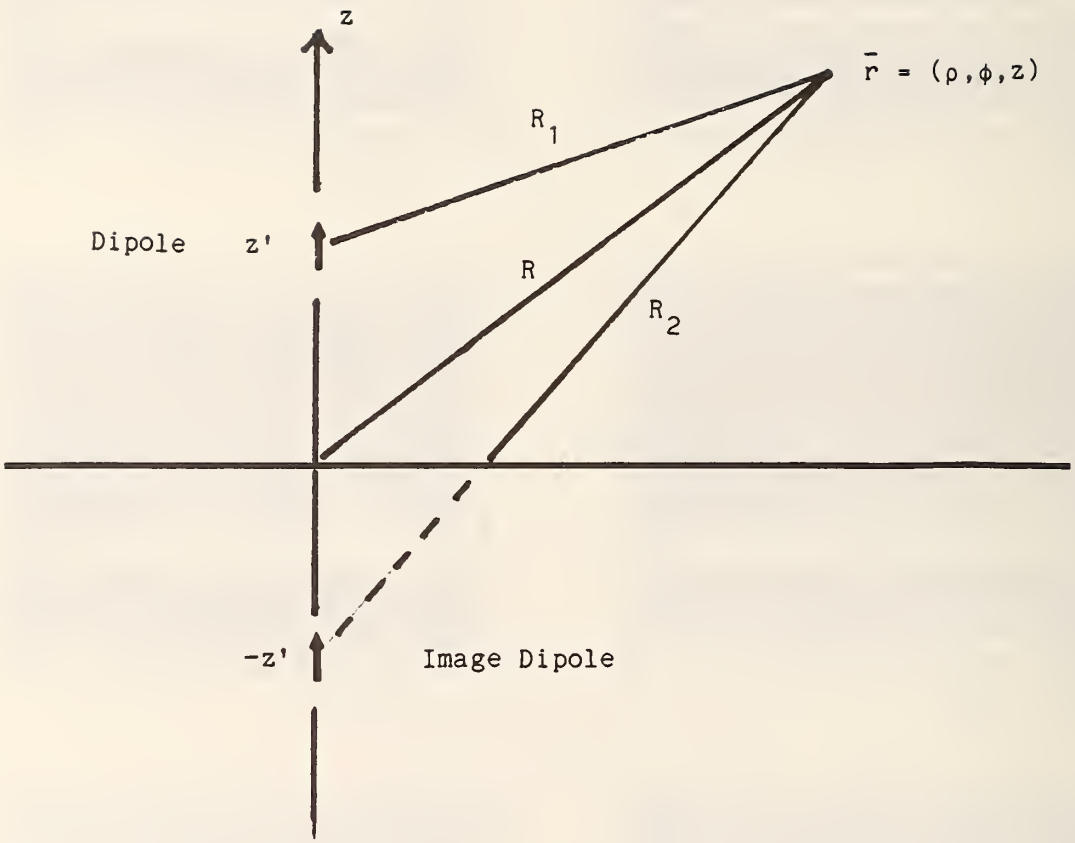

Figure 7. A dipole above a perfect ground plane and its image.

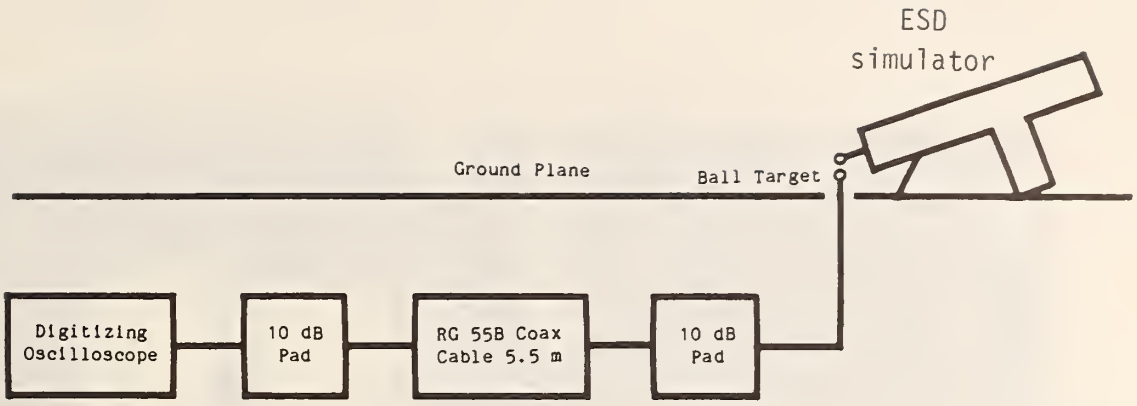

(a) For measuring current waveform.

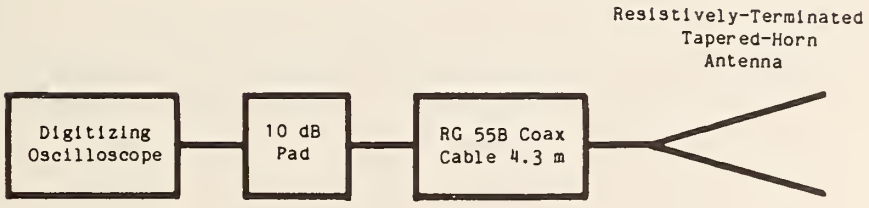

(b) For measuring electric field.

Figure 8. Measurement system schematics.

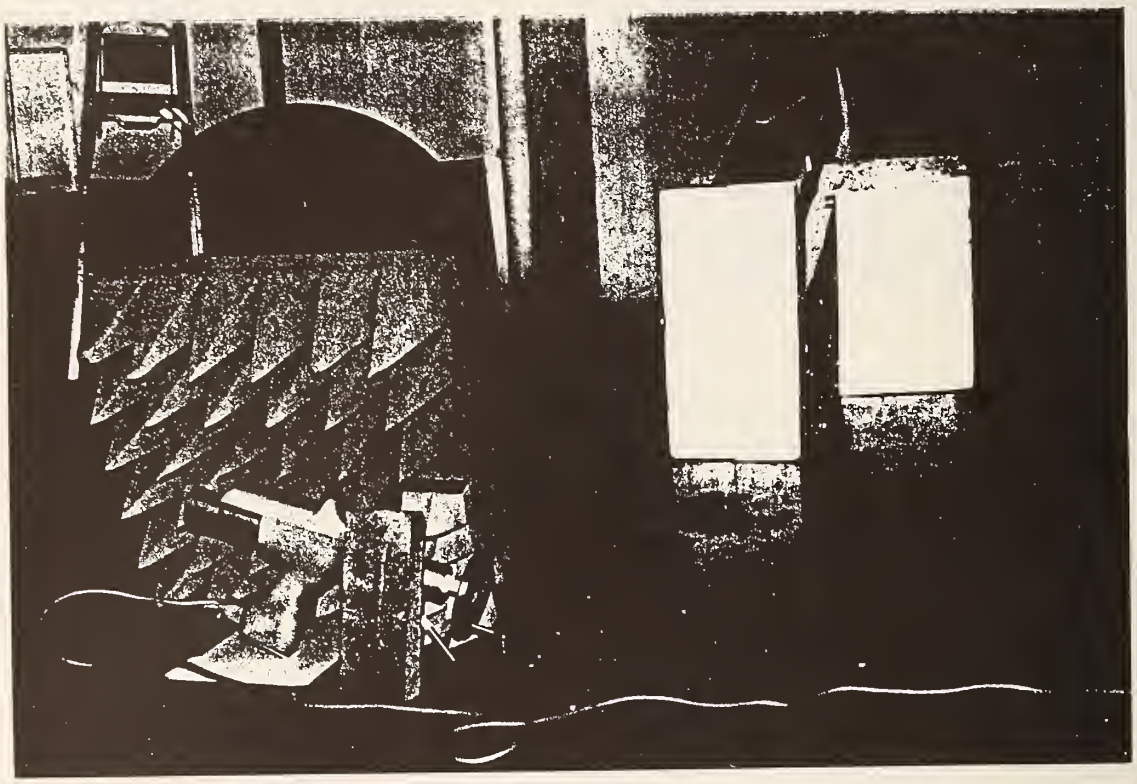

Figure 9. Coaxial ball target measurement configuration (Shield material was used to prevent radiations of the ESD simulator from interfering with the receiving system).

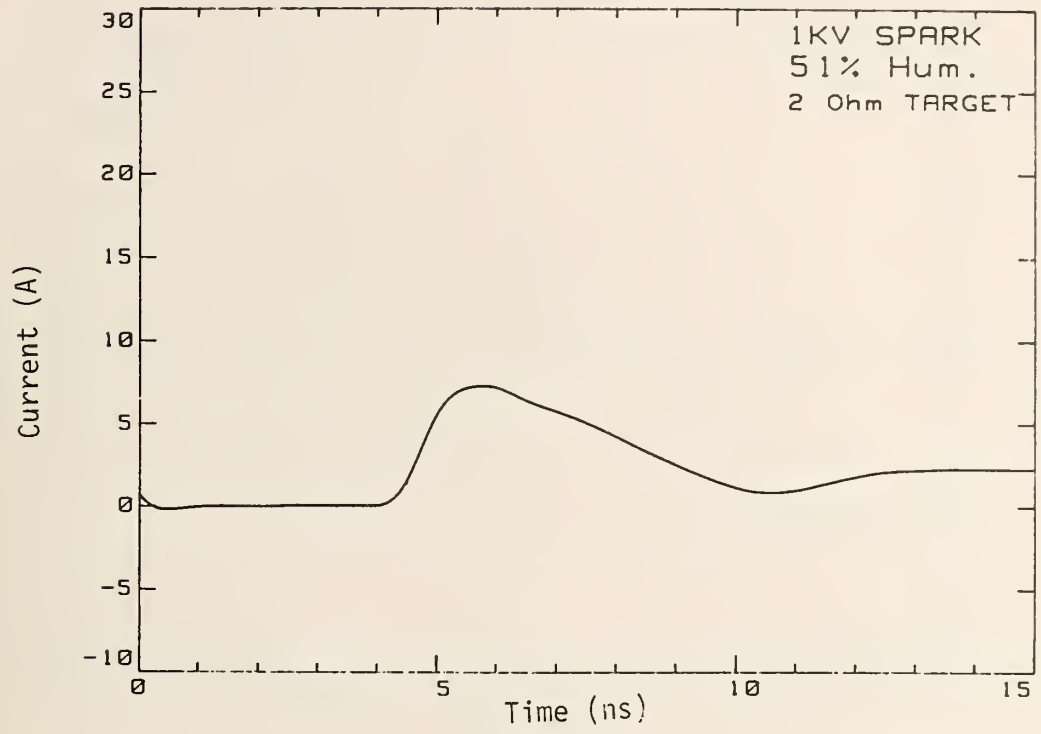

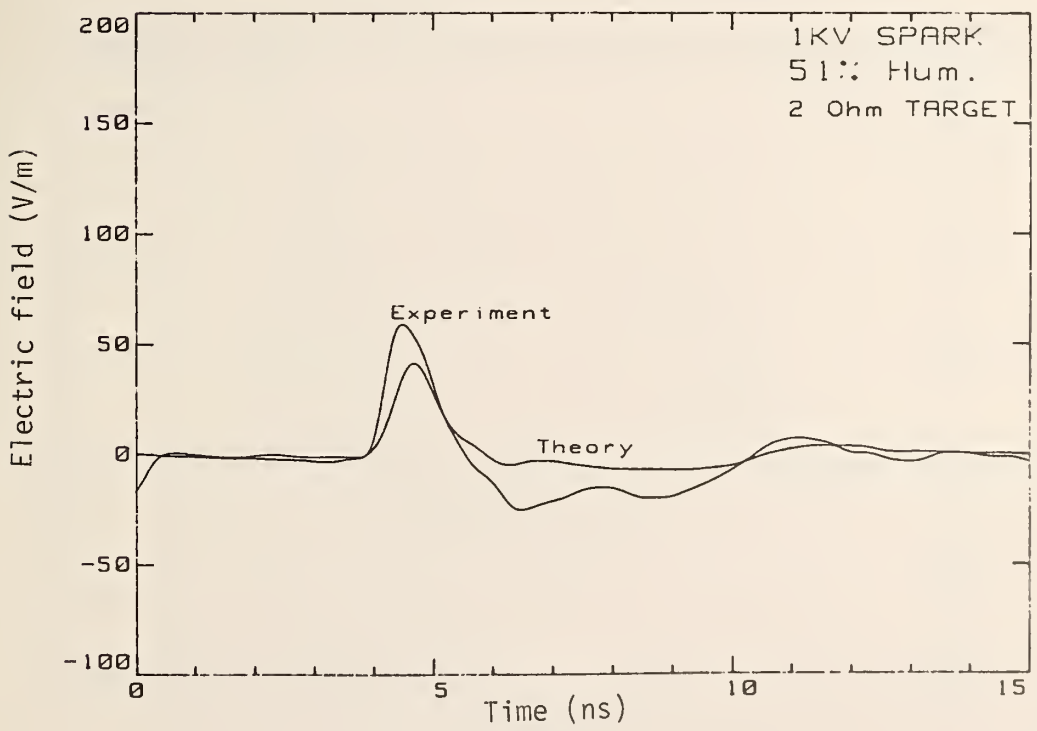

Figure 10. Coaxial ball target current and vertical electric field for a 1-kV discharge.

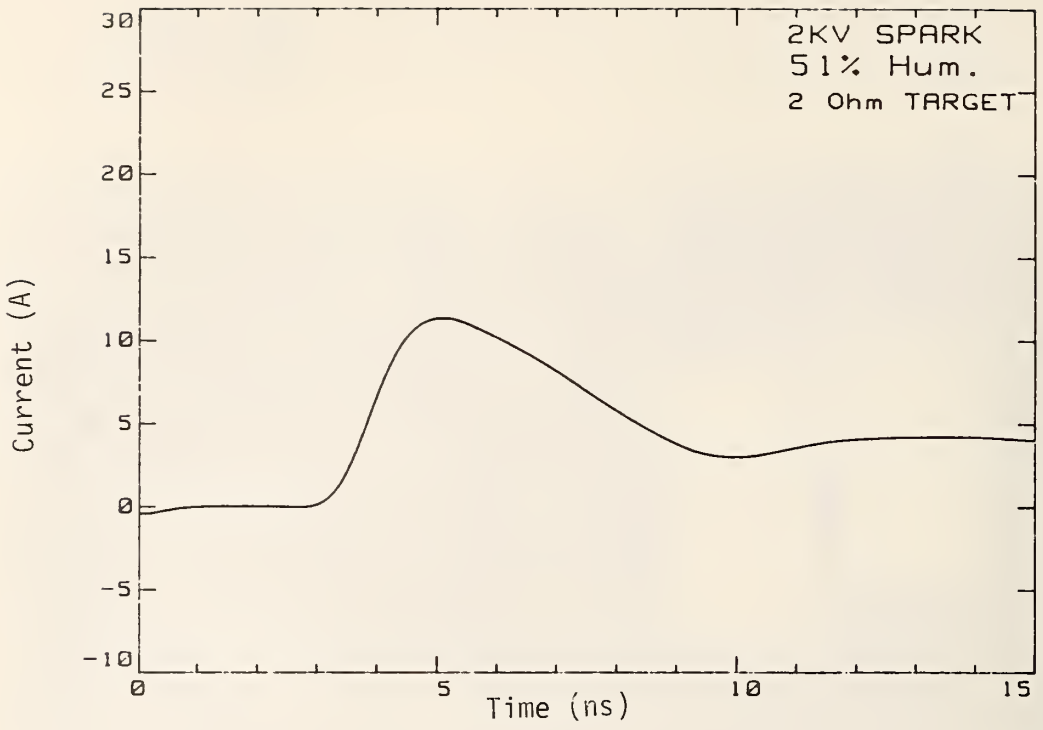

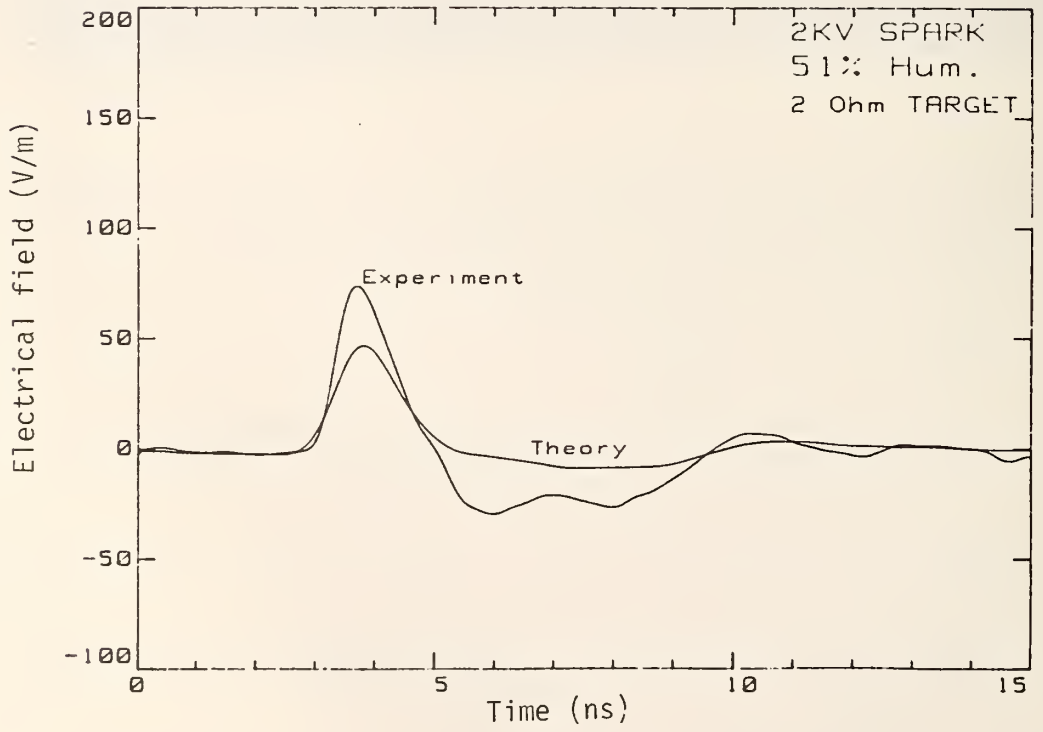

Figure 11. Coaxial ball target current and vertical electric field for a 2-kV discharge.

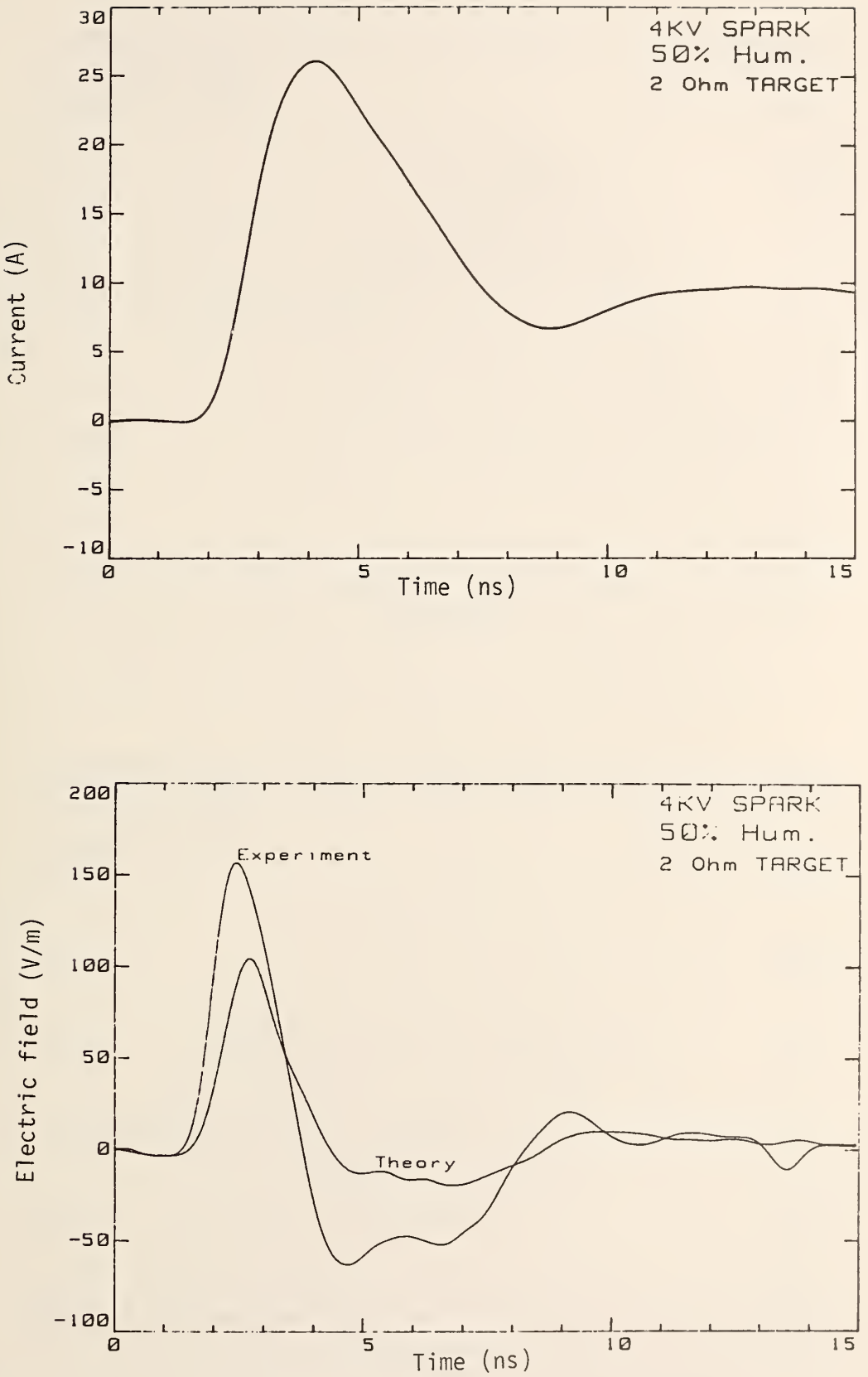

Figure 12. Coaxial ball target current and vertical electric field for a 4-kV discharge.

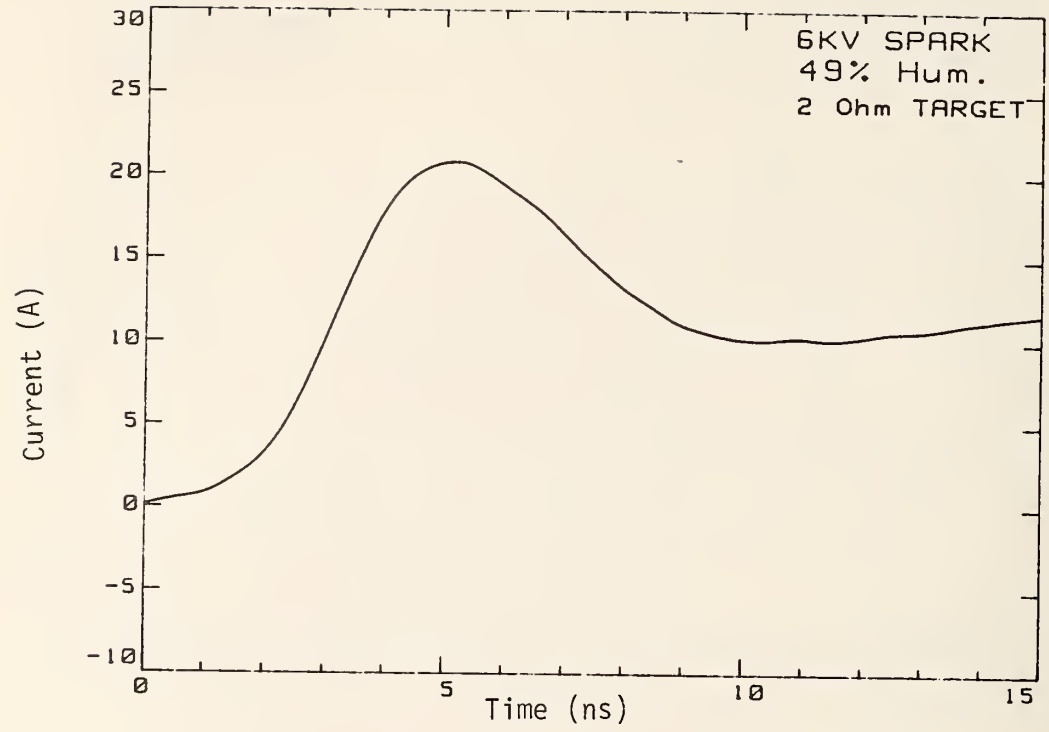

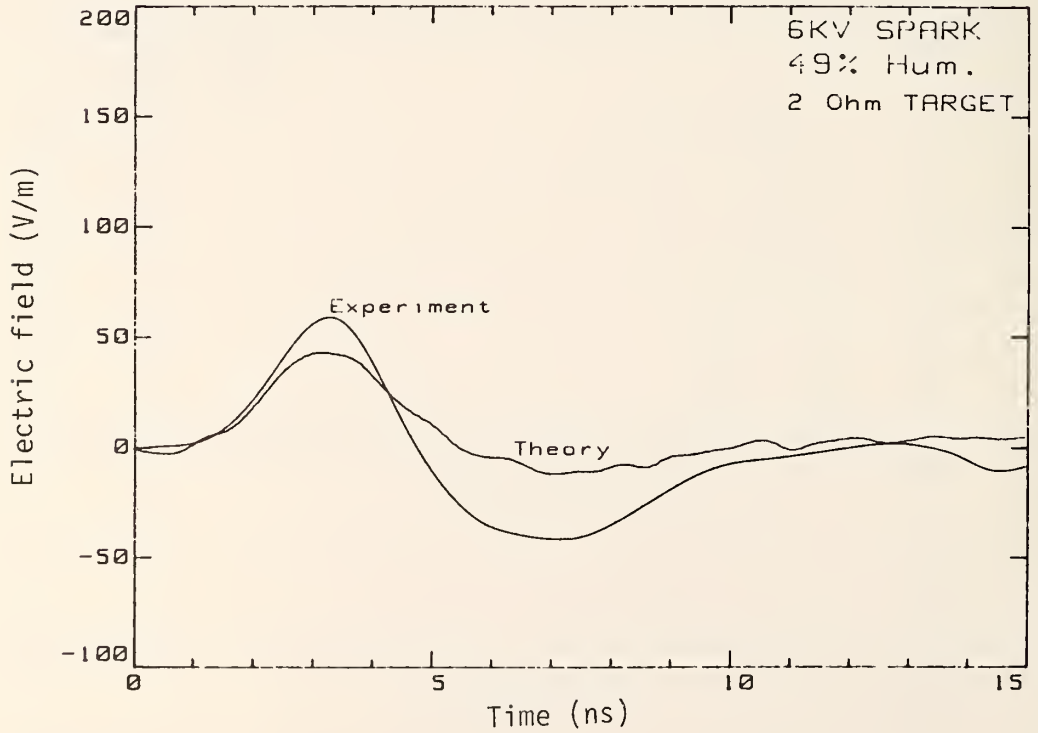

Figure 13. Coaxial ball target current and vertical electric field for a 6-kV discharge.

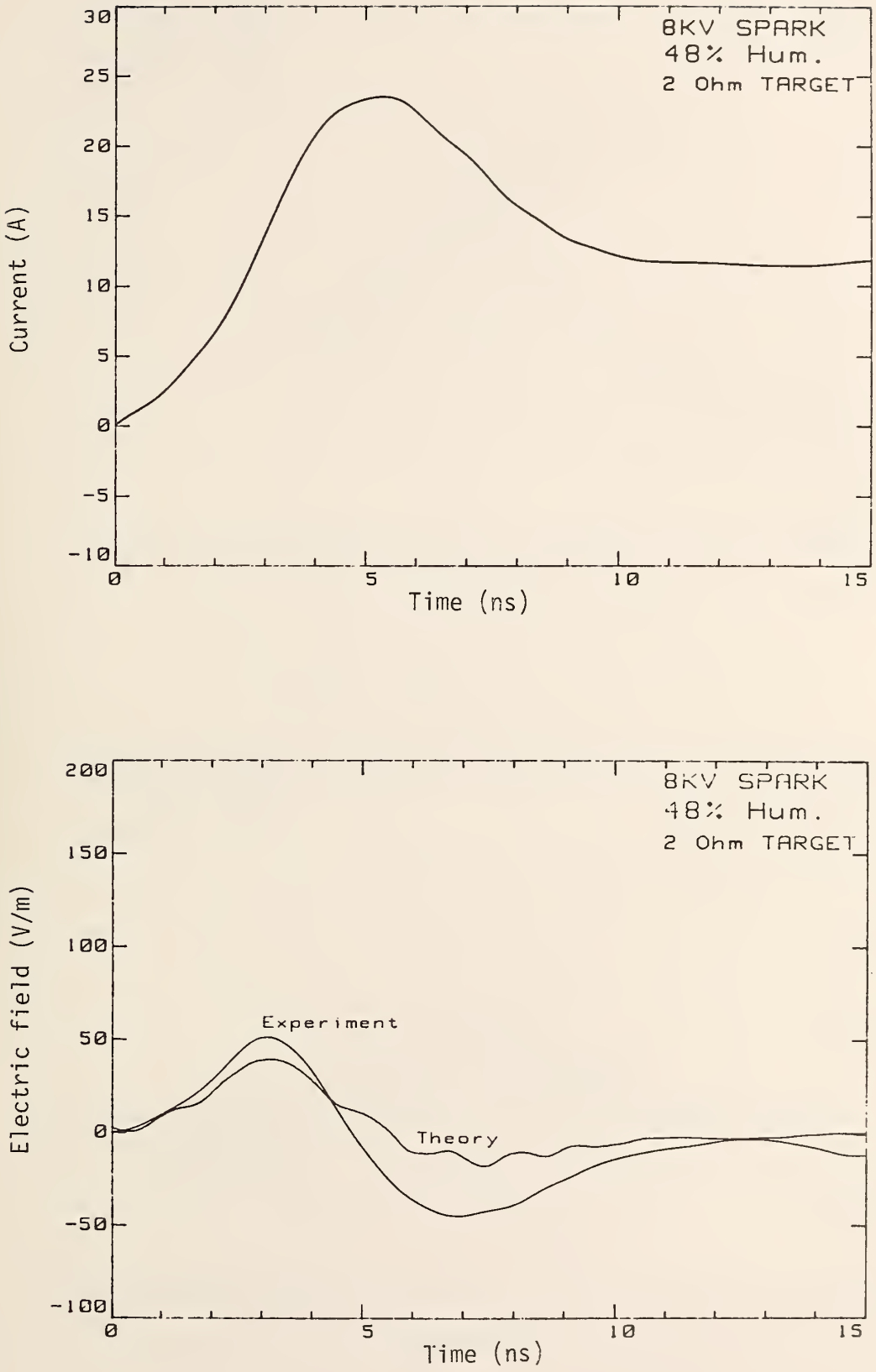

Figure 14. Coaxial ball target current and vertical electric field for a 8-kV discharge.

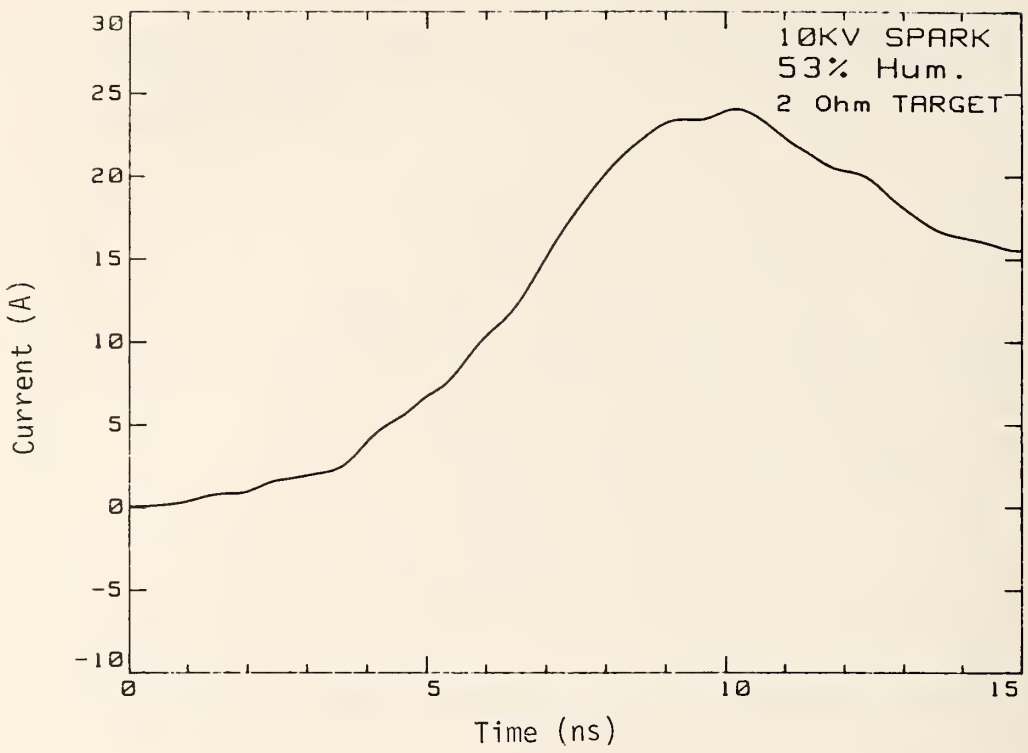

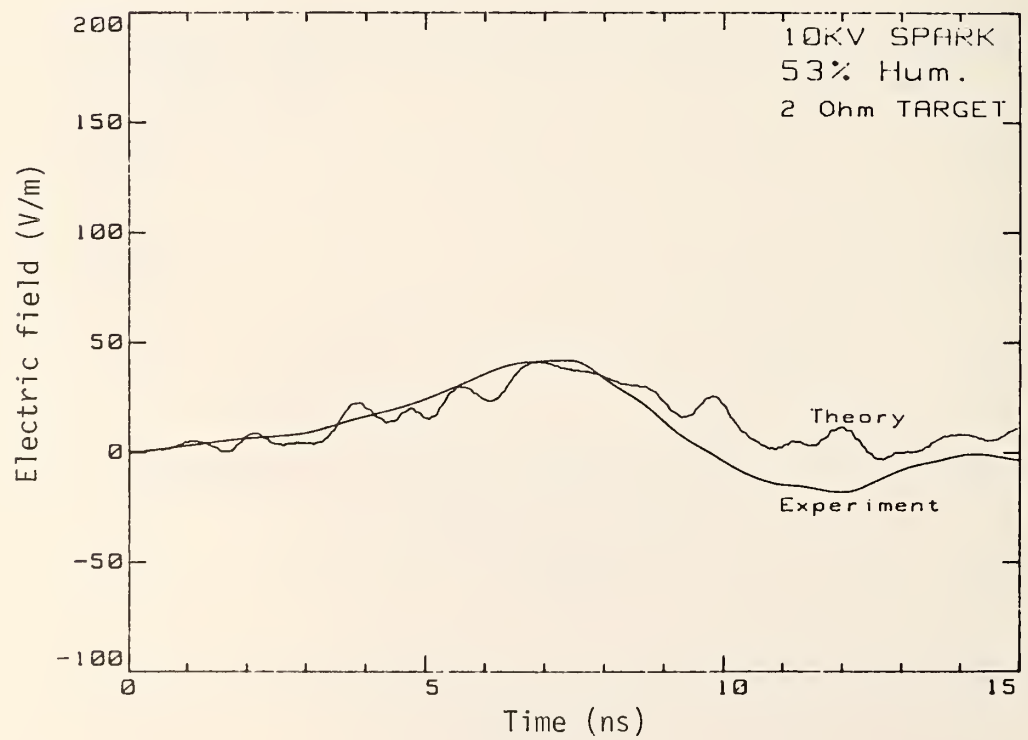

Figure 15. Coaxial ball target current and vertical electric field for a 10-kV discharge.

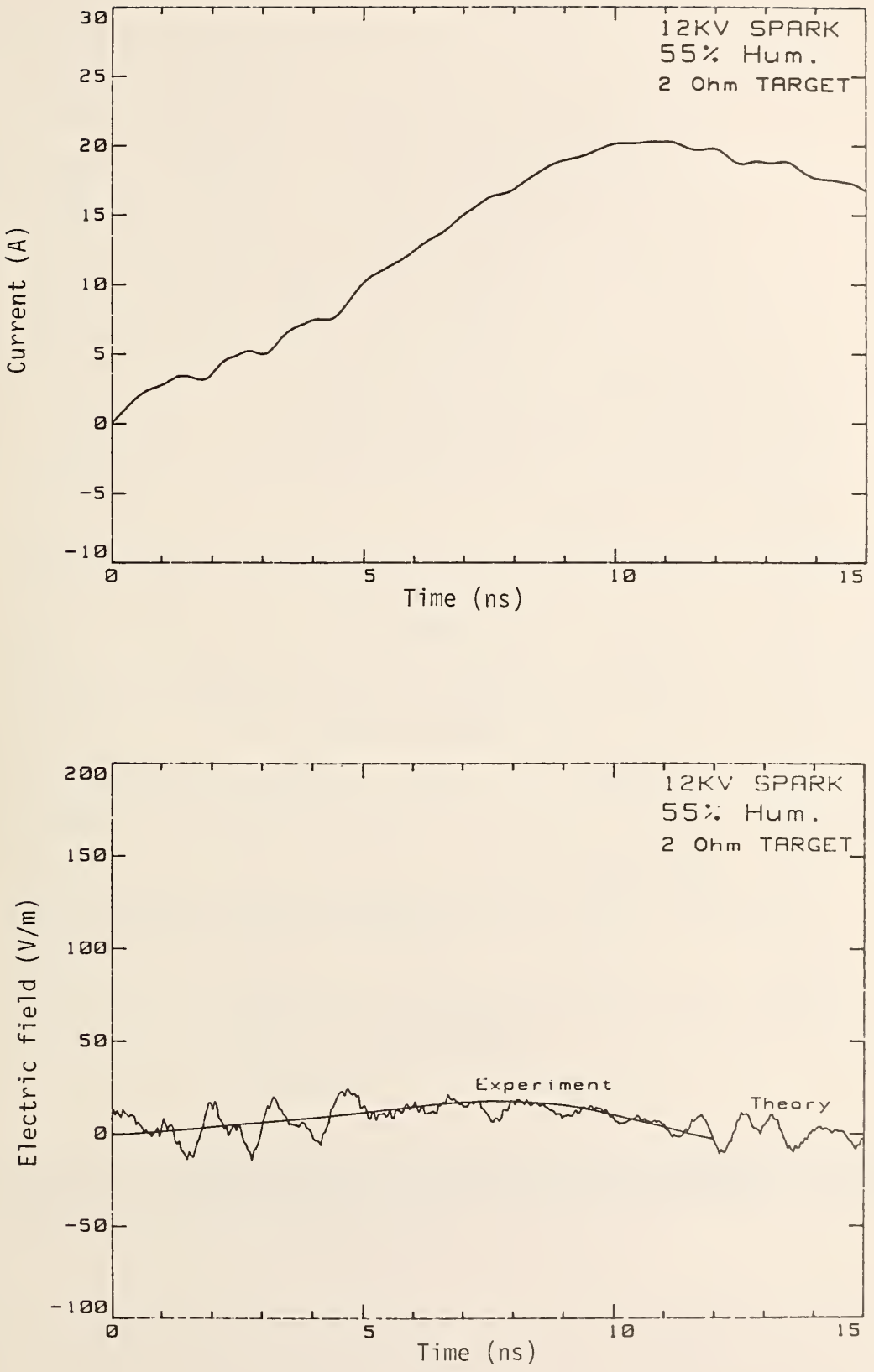

Figure 16. Coaxial ball target current and vertical electric field for a 12-kV discharge.

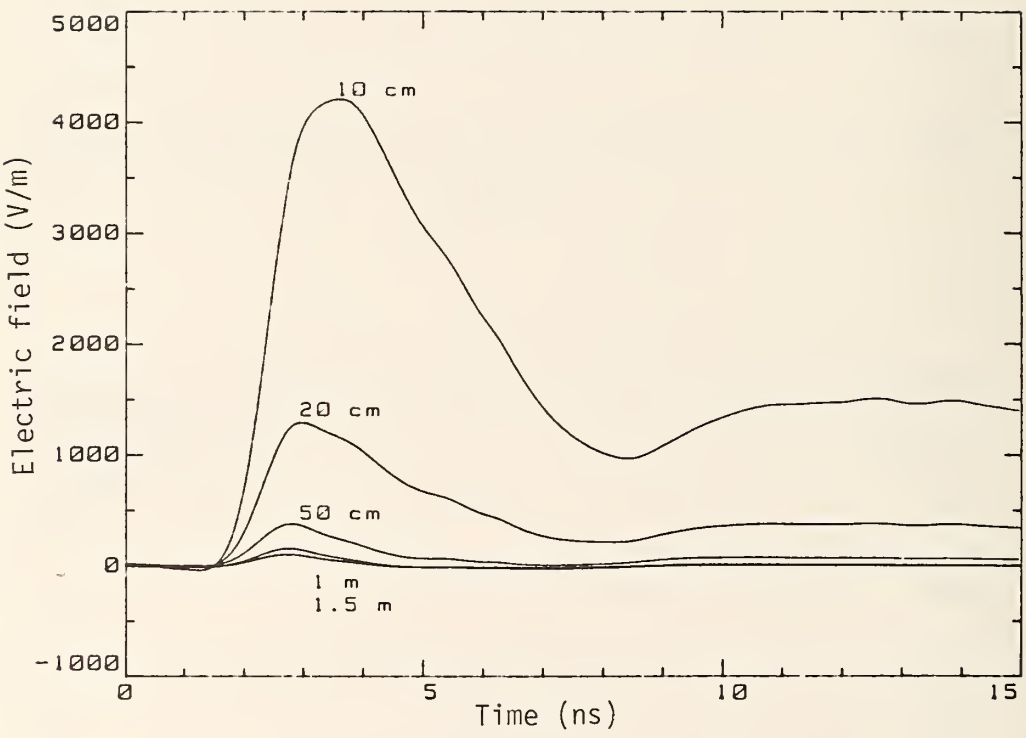

Figure 17. Predicted vertical electric field for the 4-kV discharge of fig. 12 as a function of distance to the observation point.

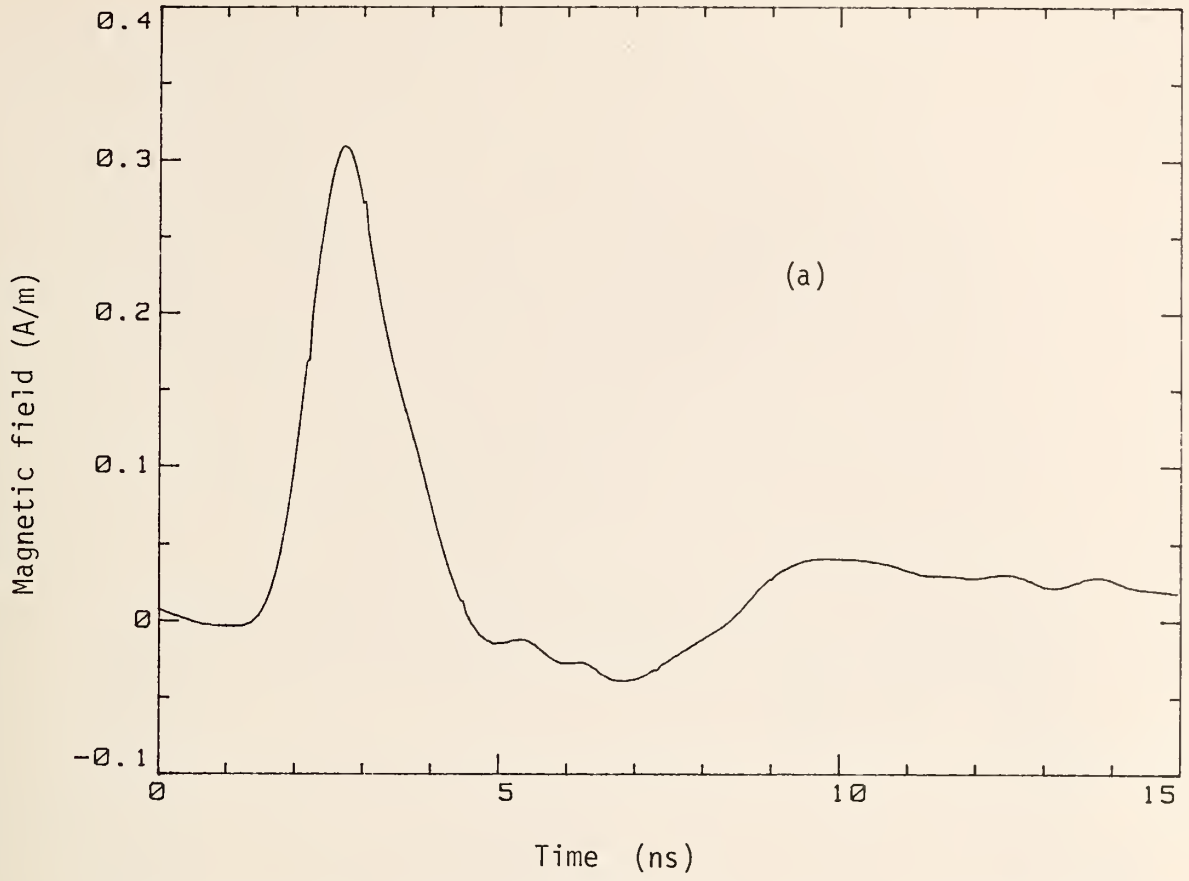

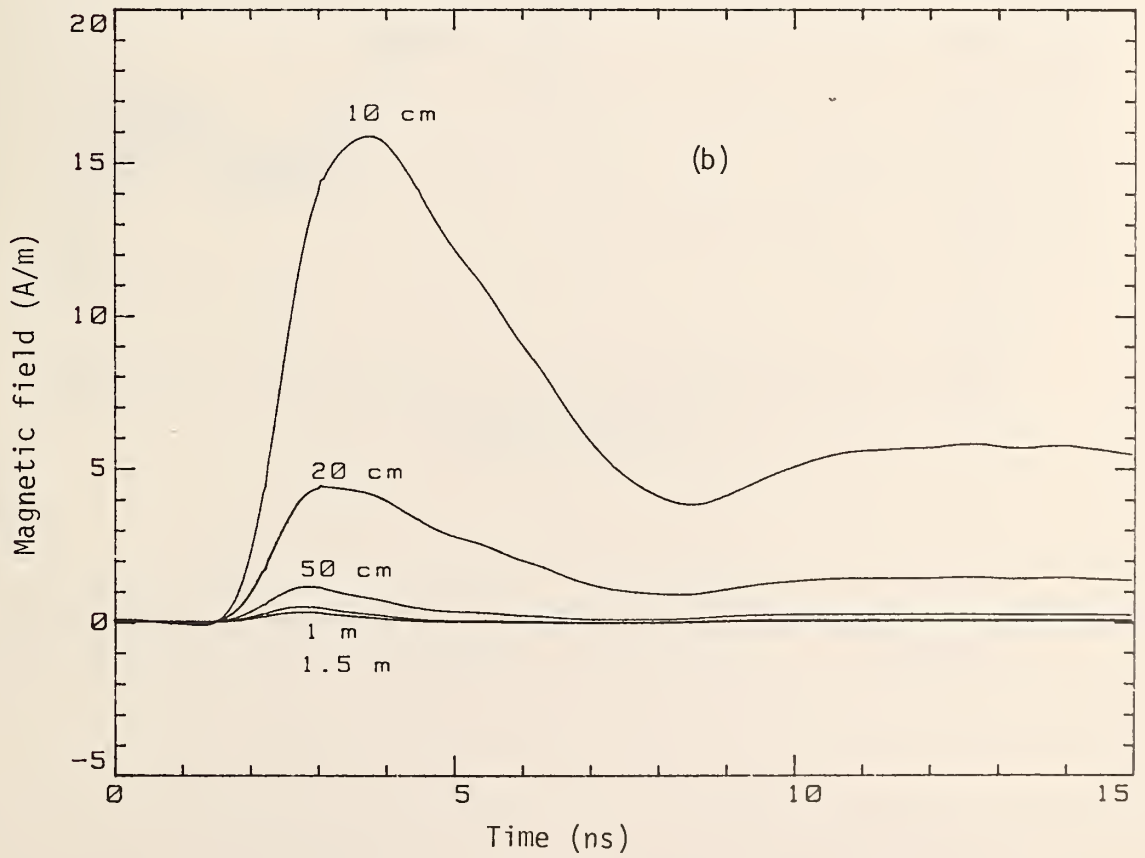

Figure 18. Predicted magnetic field for the 4-KV discharge case:
(a) with the receiving antenna at 1.5 m from the spark, and
(b) as a function of the distance to the observation point.

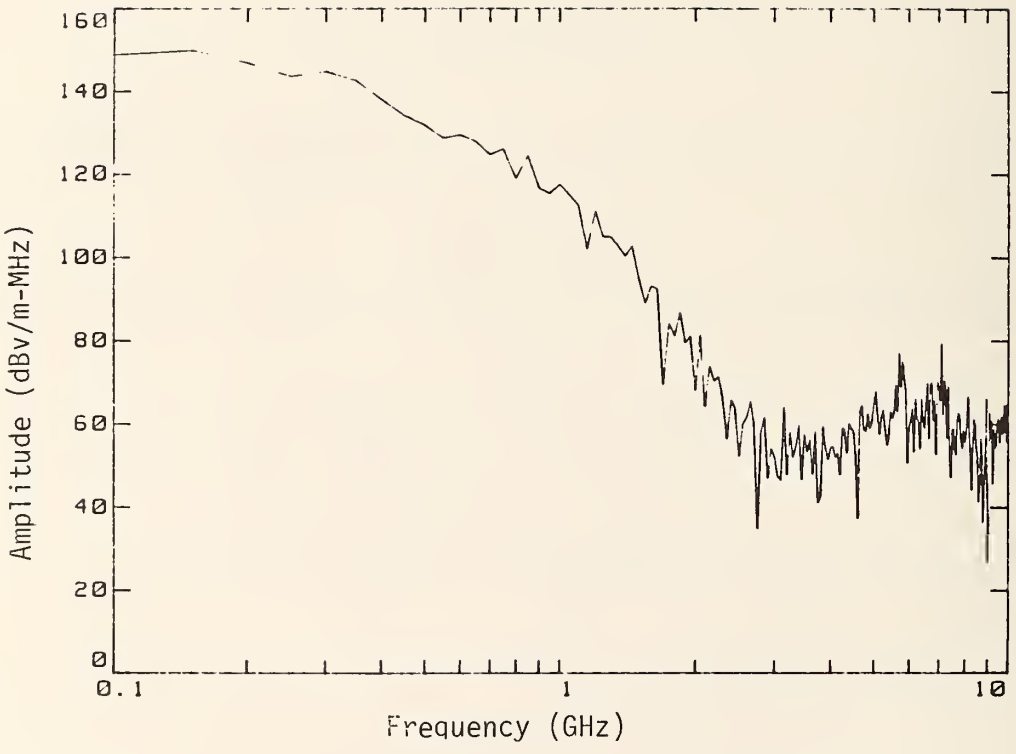

Figure 19. Spectral content for the coaxial ball target 4-KV discharge of fig. 12.

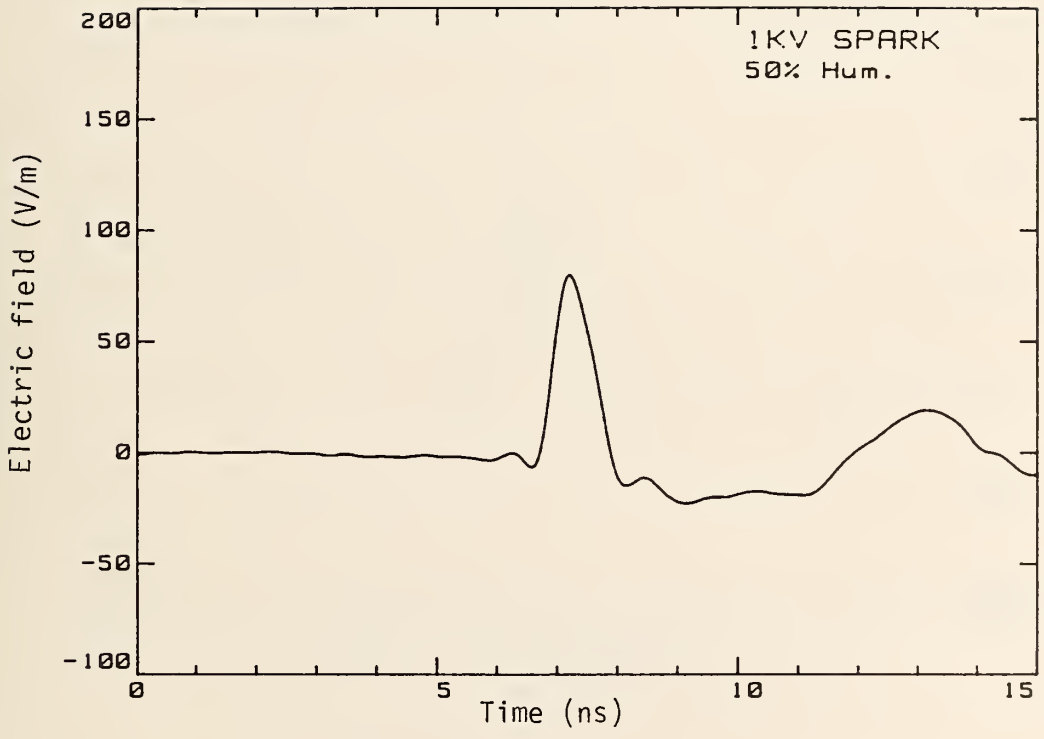

Figure 20. Vertical electric field for a 1-kV spark to a ground plane.

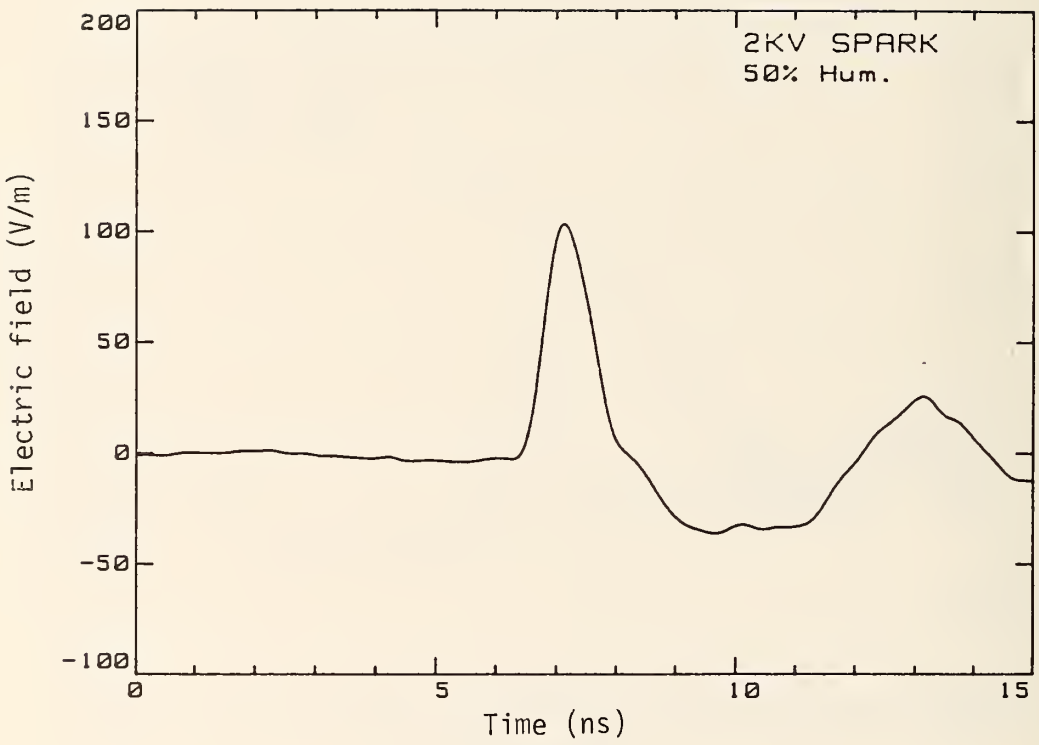

Figure 21. Vertical electric field for a 2-kV spark to a ground plane.

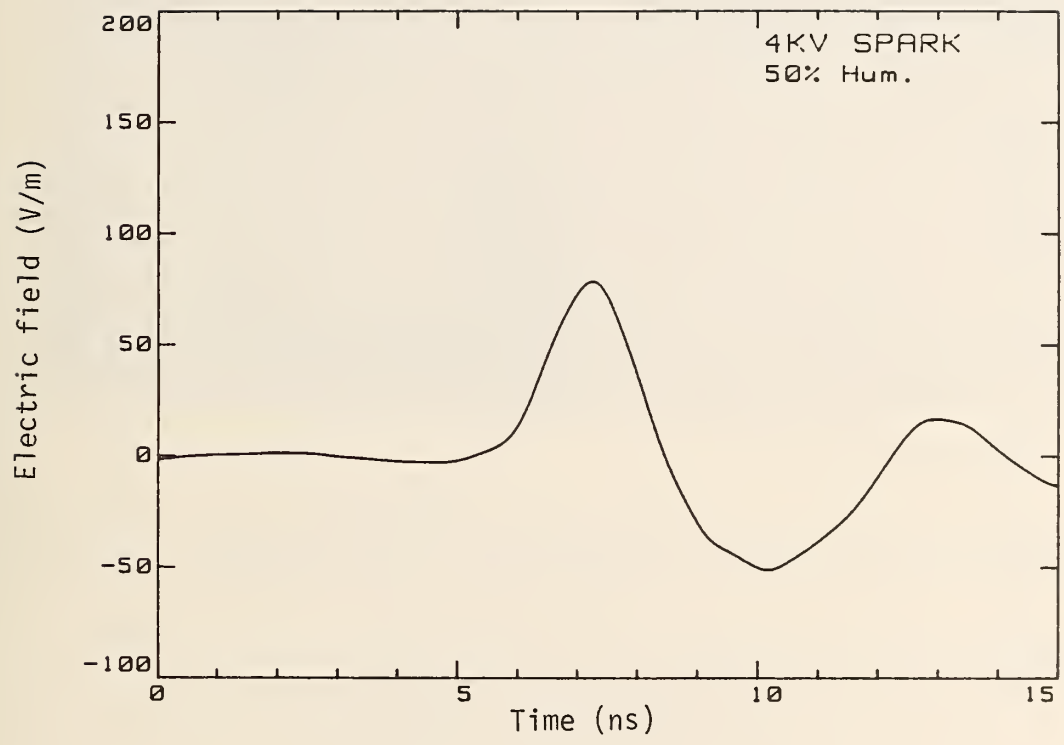

Figure 22 . Vertical electric field for a 4-kV spark to a ground plane.

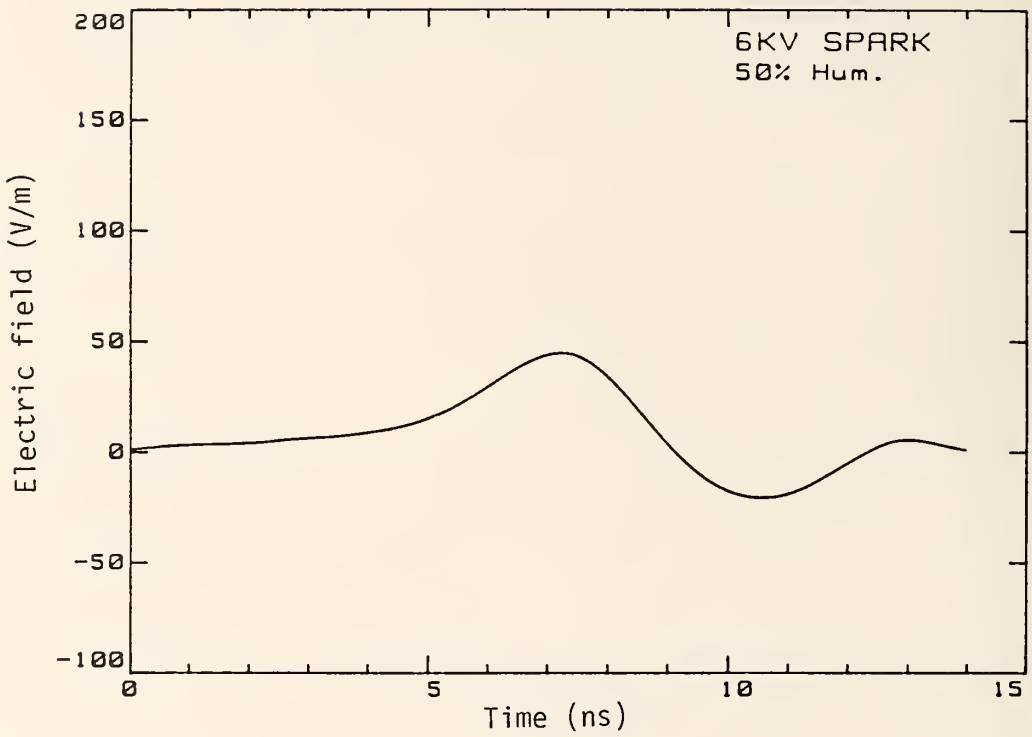

Figure 23. Vertical electric field for a 6-kV spark to a ground plane.

Figure 24. Measurement configuration for indirect radiation from a vertical square metal plate.

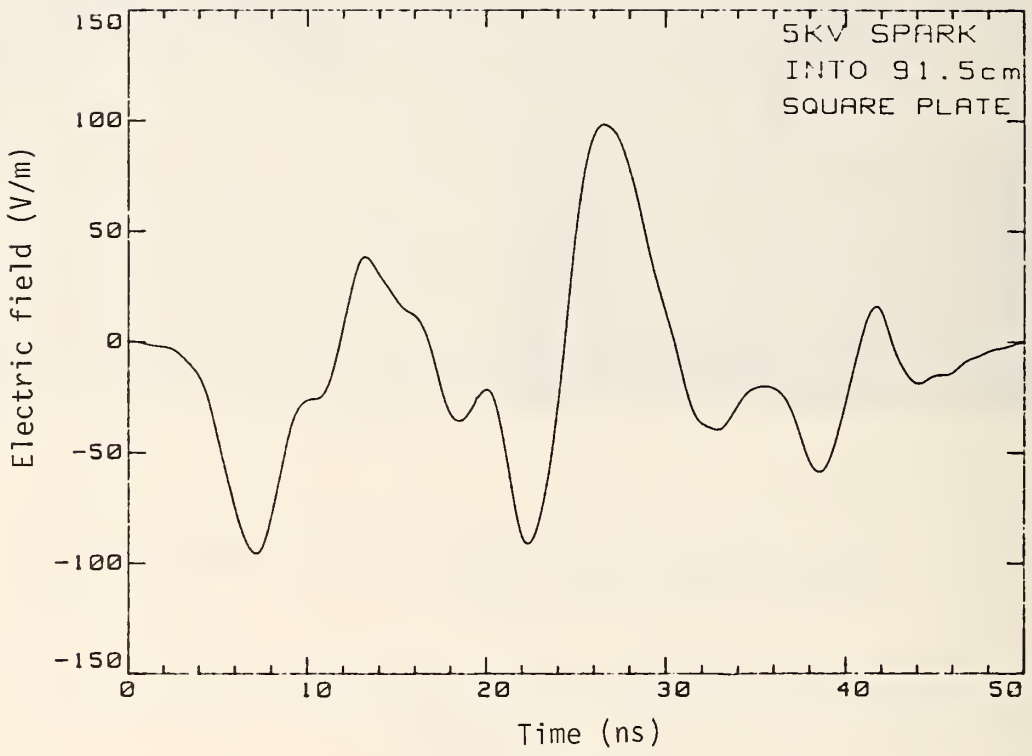

Figure 25. Vertical electric field radiated by a vertical square metal plate excited by a 5-kV spark.

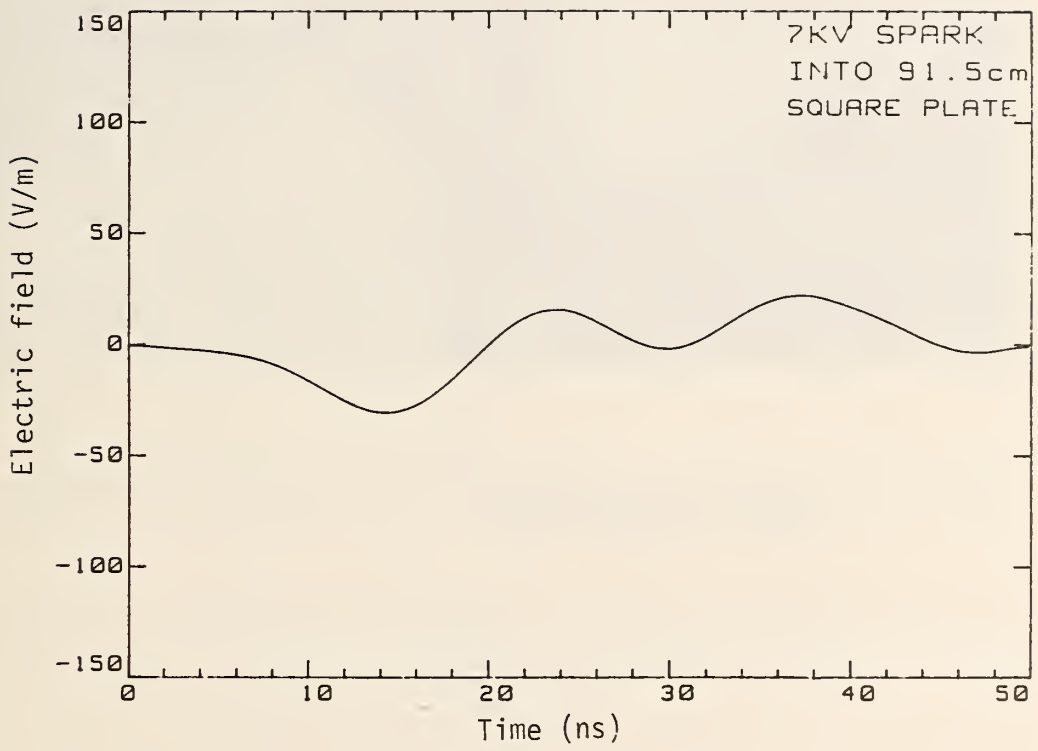

Figure 26. Vertical electric field radiated by a vertical square metal plate excited by a 7-kV spark.

Figure 27. Measurement configuration for radiation by a metal chair above a ground plane.

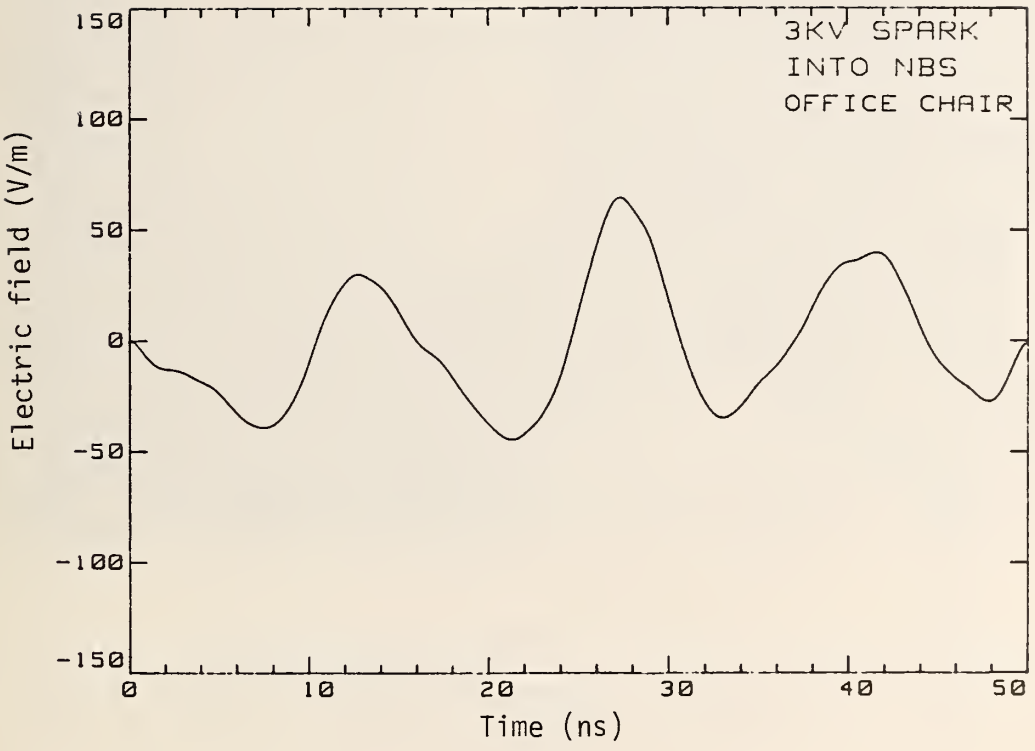

Figure 28. Vertical electric field radiated by a metal chair above a ground plane excited by a 3-kV spark.

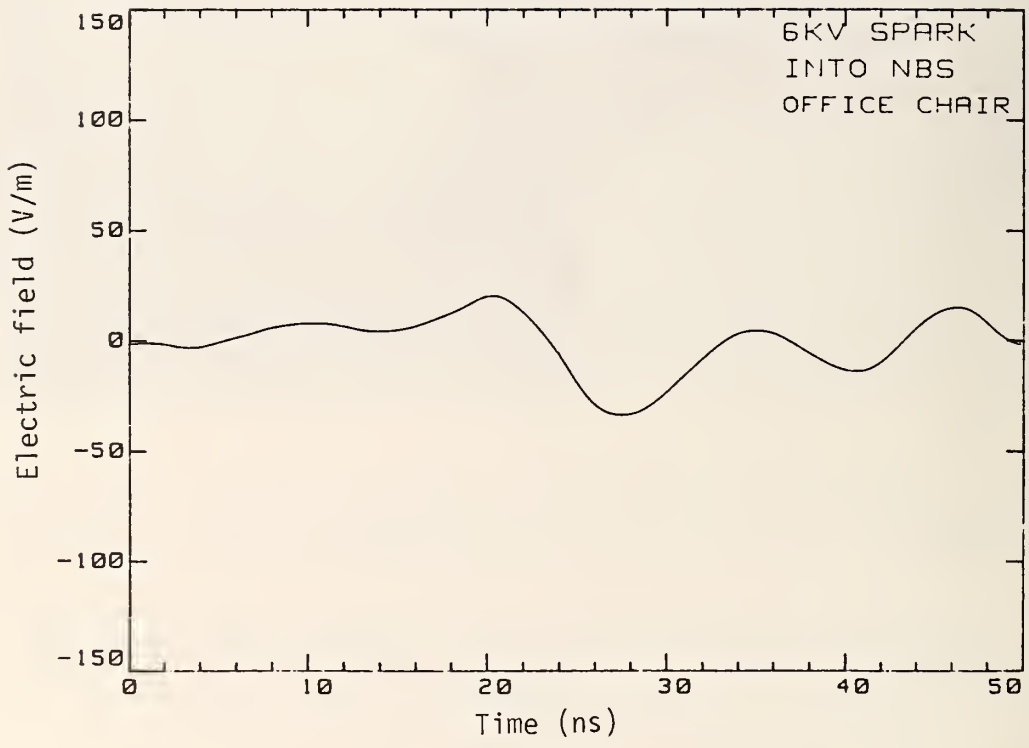

Figure 29. Vertical electric field radiated by a metal chair above a ground plane excited by a 6-kV spark.

Figure 30. Measurement configuration for radiation by a metal trash can on a ground plane.

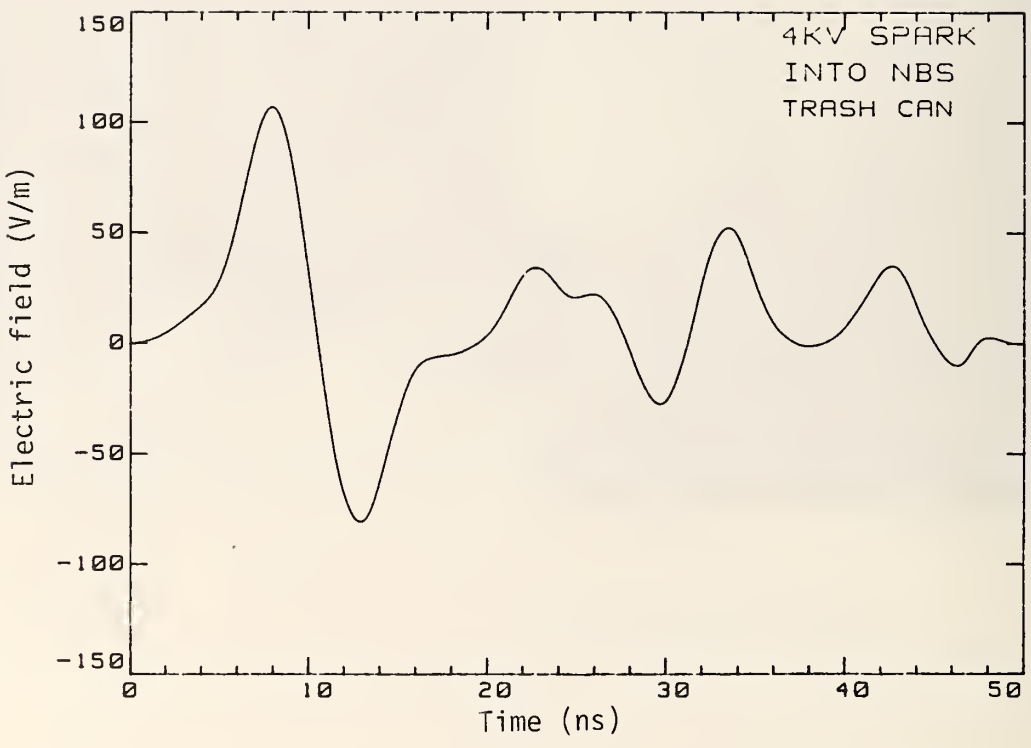

Figure 31. Vertical electric field radiated by a metal trash can excited by a 4-kV spark.

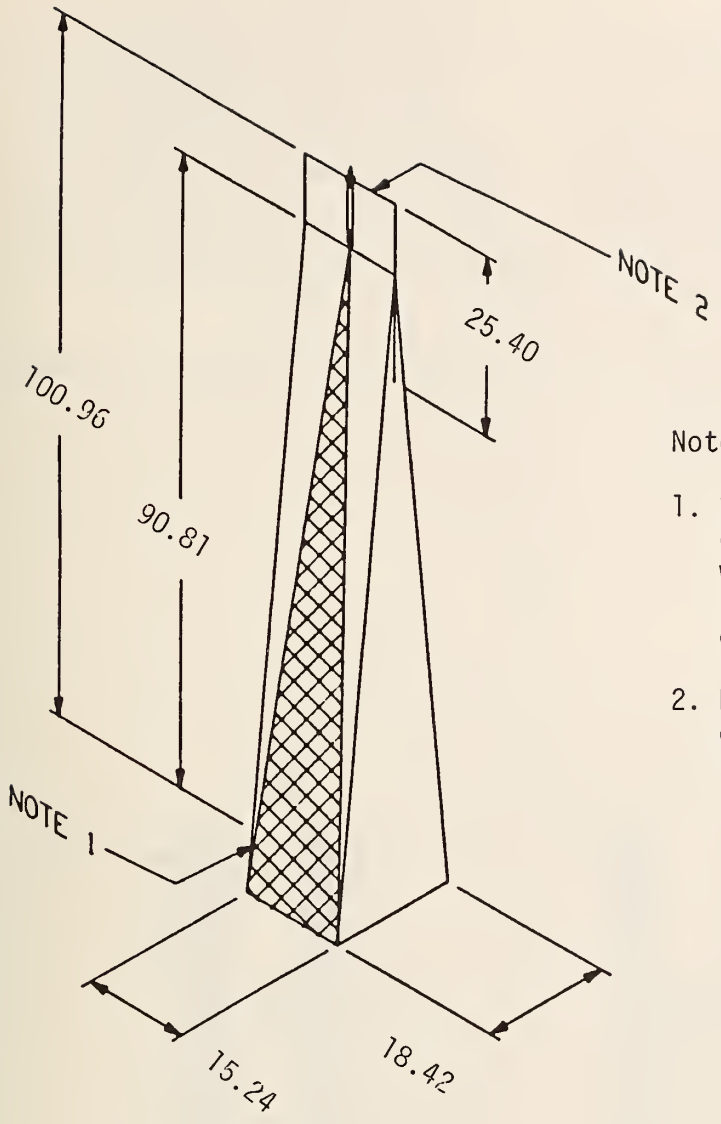

Note:

1. Two,single-sided, G10 copper-clad glass epoxy PC boards, separated with a wedge of styroform extruded polystyrene insulation (copper side down).

2. Double-sided, G10 copper clad glass epoxy PC board, with details shown in fig. 33.

Figure 32. The UHF antenna (NBS 200-1) for measuring the broadband electric fields: dimensions in the figure are in centimeters.

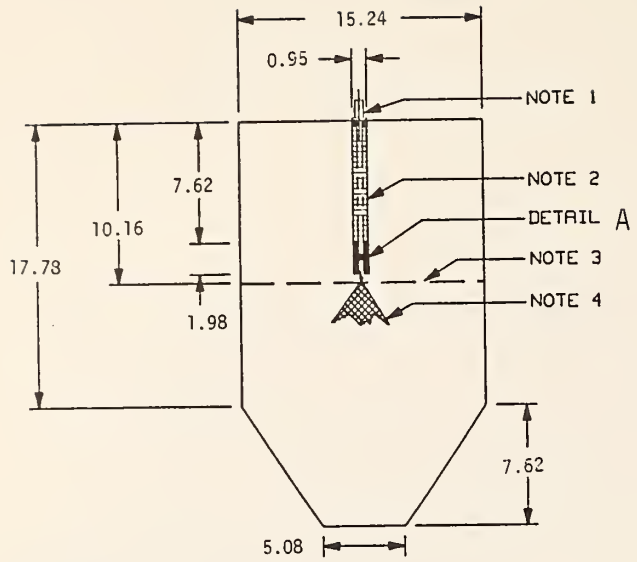

Note:

1. SMA connector for 0.36 cm semi-rigid cable.
2. 0.36 cm semi-rigid cable wrapped with alternating ferrite cores of Q1,Q2, and Q3 material types with typical dimensions of 0.97 cm outer diameter, 0.74 cm inner diameter, and 0.33 cm thickness.
3. PC board fits into 15.24 cm slot in foam wedge.
4. Single side copper clad antenna piece

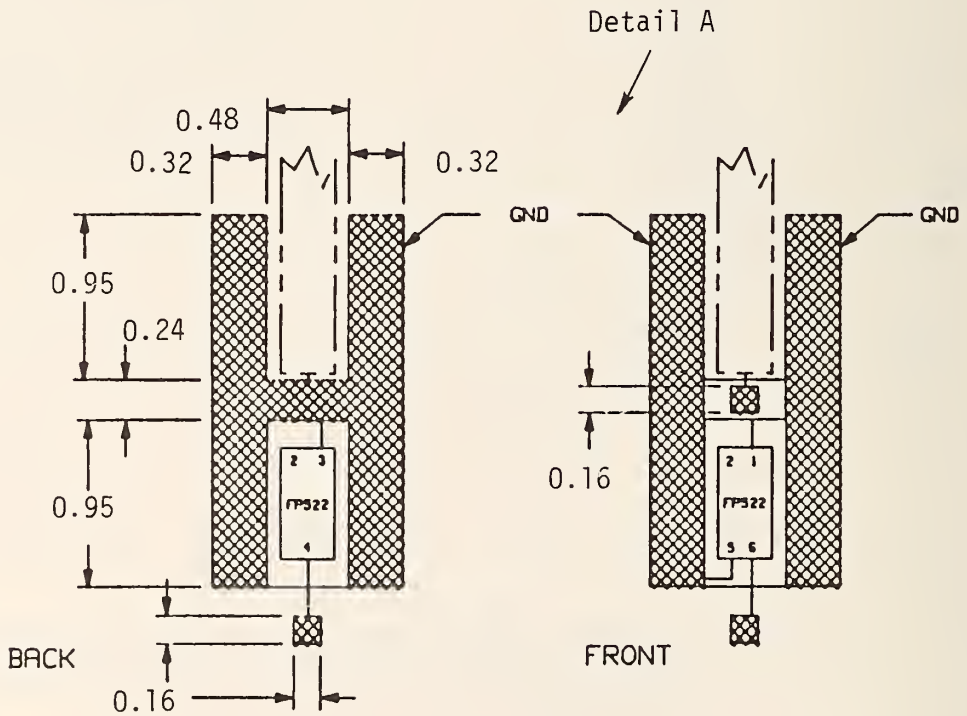

Figure 33. Construction details of the pulse transformer in the NBS 200-1 antenna (all dimensions in centimeters).

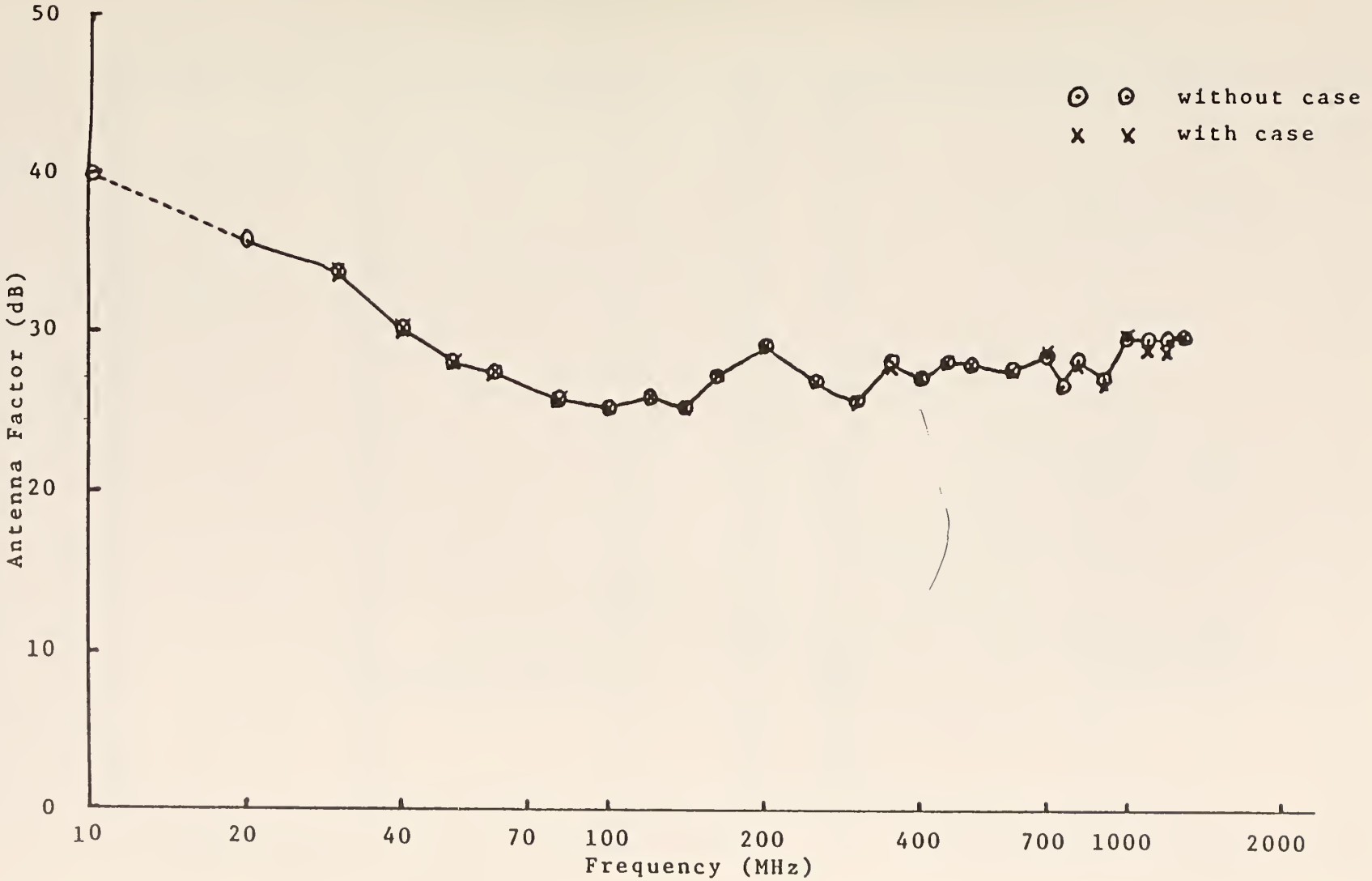

Figure 34. Comparison of the frequency response of the NBS 200-1 antenna with and without the Kydex jacket.

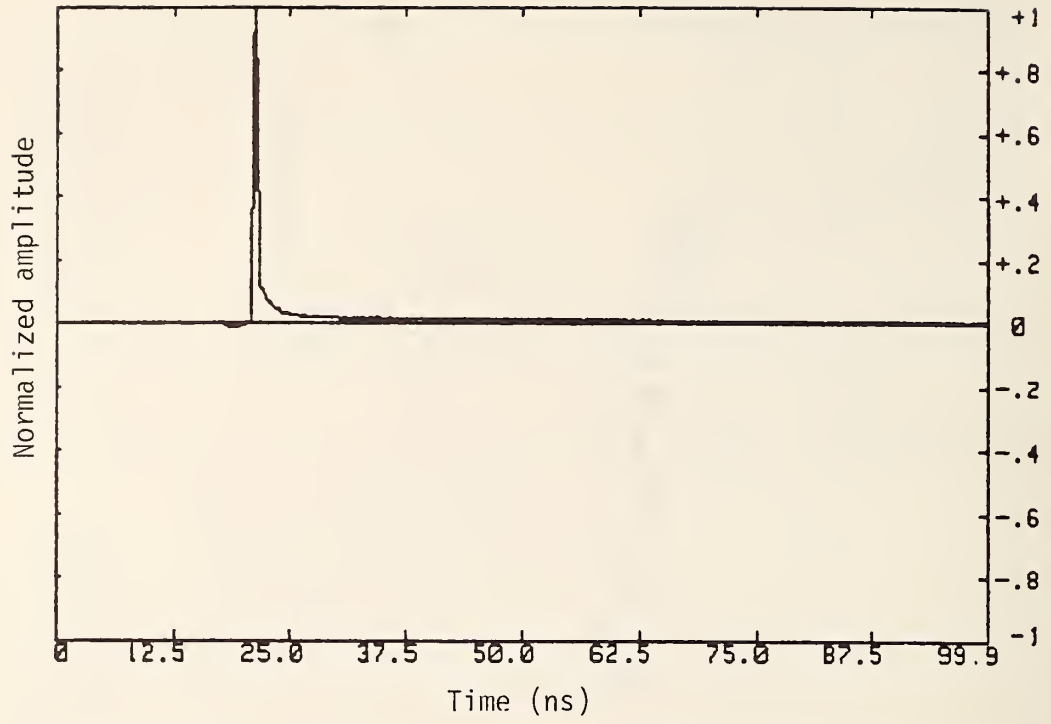

Figure 35. Normalized amplitude of the transmitting pulse.

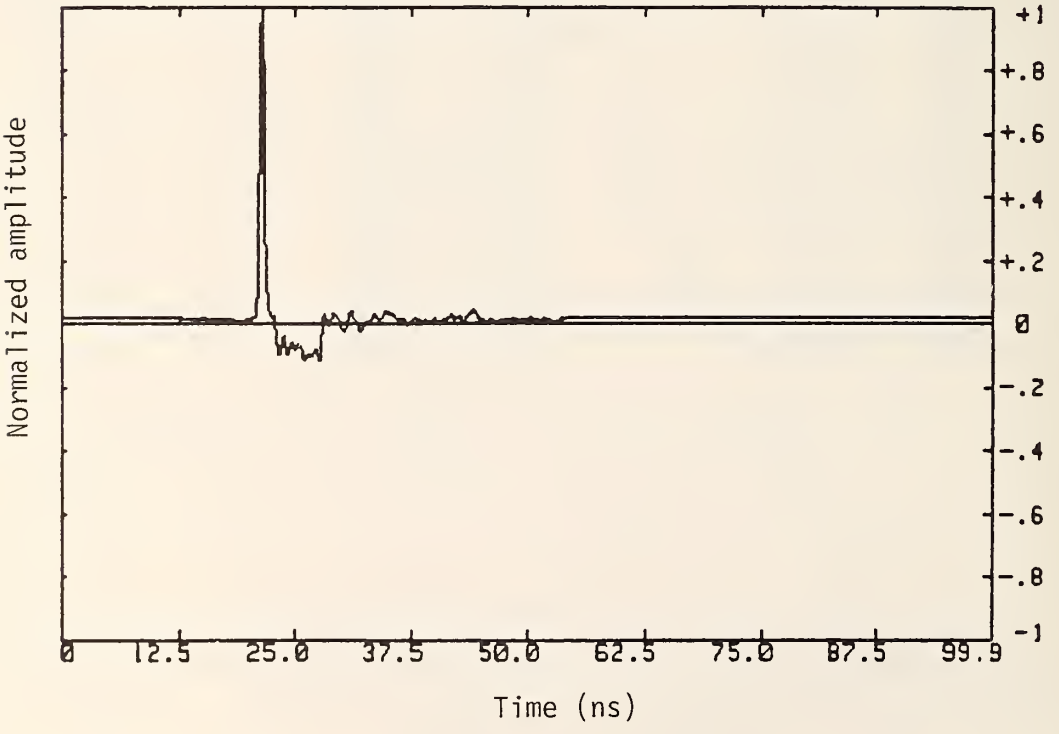

Figure 36. Response of the NBS 200-1 antenna to the transmitting pulse shown in fig. 35.

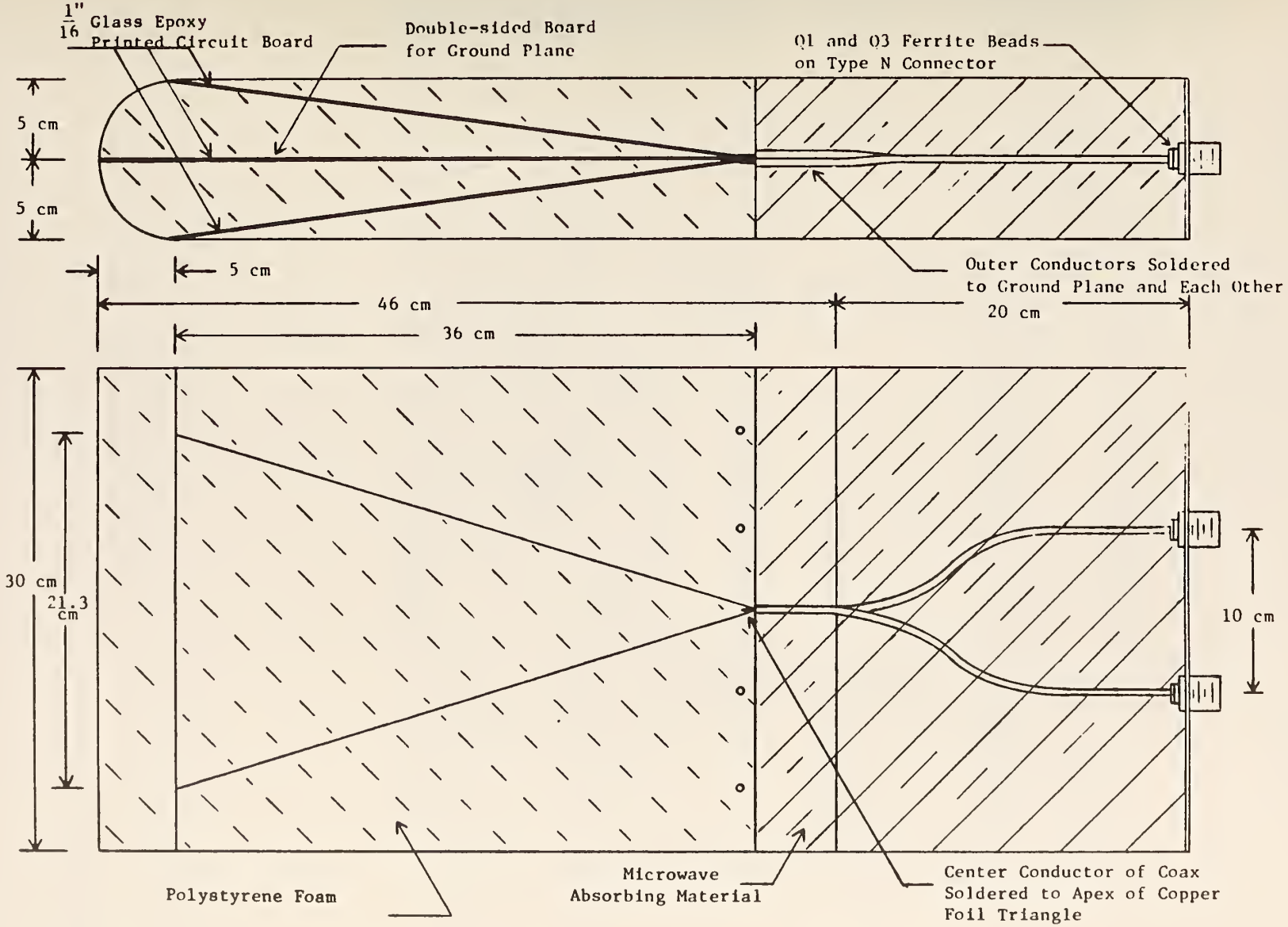

Figure 37. The microwave horn antenna, NBS 50-2.

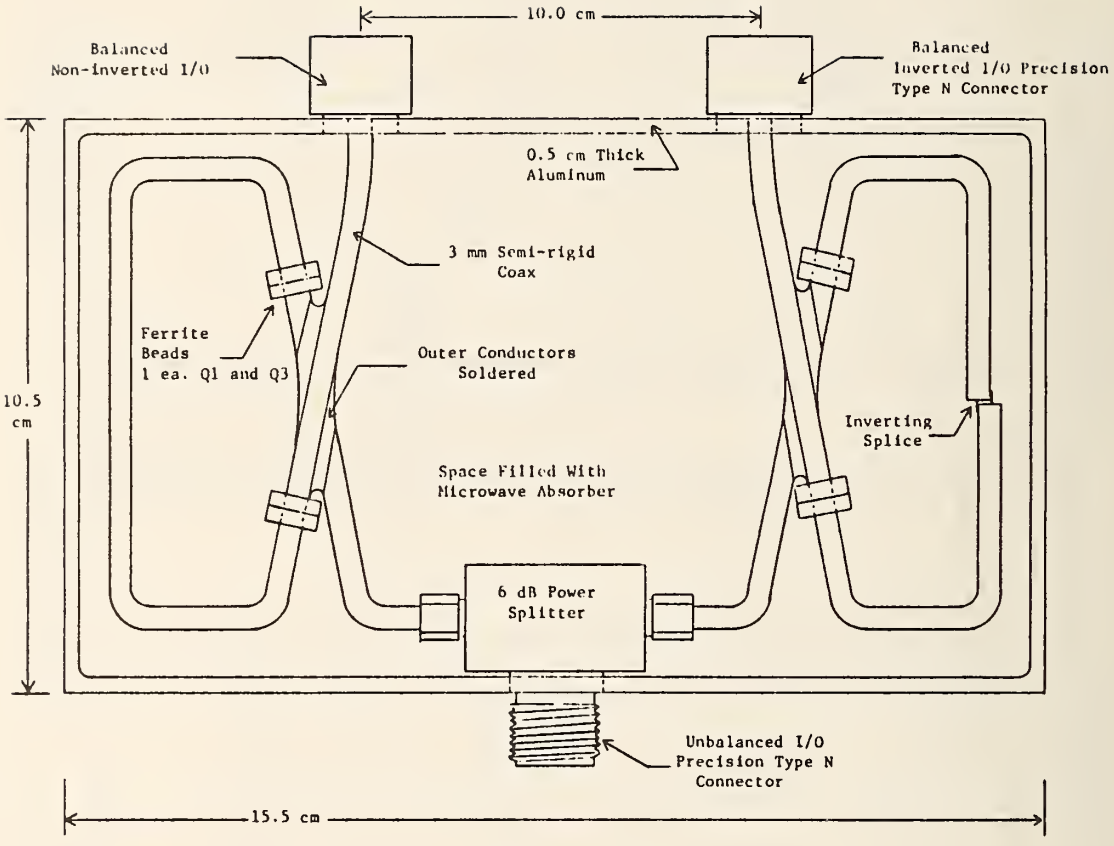

Figure 38. The broadband balun used for the antenna in fig.37.

NBS-114A (REV. 2-8C)

U.S. DEPT. OF COMM. **BIBLIOGRAPHIC DATA SHEET** *(See instructions)*	1. PUBLICATION OR REPORT NO. NBS/TN-1314	2. Performing Organ. Report No.	3. Publication Date February 1988

4. TITLE AND SUBTITLE

ELECTROMAGNETIC FIELDS RADIATED FROM ELECTROSTATIC DISCHARGES--
THEORY AND EXPERIMENT

5. AUTHOR(S)

P. F. Wilson, A. R. Ondrejka, M. T. Ma, and J. M. Ladbury

6. PERFORMING ORGANIZATION *(If joint or other than NBS, see instructions)*

NATIONAL BUREAU OF STANDARDS
DEPARTMENT OF COMMERCE
WASHINGTON, D.C. 20234

7. Contract/Grant No.

8. Type of Report & Period Covered

9. SPONSORING ORGANIZATION NAME AND COMPLETE ADDRESS *(Street, City, State, ZIP)*

10. SUPPLEMENTARY NOTES

☐ Document describes a computer program; SF-185, FIPS Software Summary, is attached.

11. ABSTRACT *(A 200-word or less factual summary of most significant information. If document includes a significant bibliography or literature survey, mention it here)*

The fields radiated by electrostatic discharges (ESD) are studied both theoretically and experimentally. The ESD spark is modeled theoretically as an electrically short, time dependent, linear dipole situated above an infinite ground plane. Experimentally, sparks of varying voltages are generated by a commercially available simulator and used to excite a number of targets including (1) the extended inner conductor of a coaxial cable mounted in a ground plane, (2) direct discharges to a ground plane, (3) indirect radiation from a large metal plate, (4) a metal chair over a ground plane, and (5) a metal trash can. Results show that relatively low-voltage sparks (2-4 kV) excite the strongest radiated fields. This suggests that the spark fields can pose a significant interference threat to electronic equipment into the gigahertz range.

12. KEY WORDS *(Six to twelve entries; alphabetical order; capitalize only proper names; and separate key words by semicolons)*

electrostatic discharge; pulsed current; radiated electric field; radiated magnetic field; spectrum; time-domain technique

13. AVAILABILITY

☒ Unlimited

☐ For Official Distribution. Do Not Release to NTIS

☒ Order From Superintendent of Documents, U.S. Government Printing Office, Washington, D.C. 20402.

☐ Order From National Technical Information Service (NTIS), Springfield, VA. 22161

14. NO. OF PRINTED PAGES

72

15. Price

USCOMM-DC 6043-P80

U.S. GOVERNMENT PRINTING OFFICE 1988—574-791 85,109 REGION NO. 8

NBS Technical Publications

Periodical

Journal of Research—The Journal of Research of the National Bureau of Standards reports NBS research and development in those disciplines of the physical and engineering sciences in which the Bureau is active. These include physics, chemistry, engineering, mathematics, and computer sciences. Papers cover a broad range of subjects, with major emphasis on measurement methodology and the basic technology underlying standardization. Also included from time to time are survey articles on topics closely related to the Bureau's technical and scientific programs. Issued six times a year.

Nonperiodicals

Monographs—Major contributions to the technical literature on various subjects related to the Bureau's scientific and technical activities.

Handbooks—Recommended codes of engineering and industrial practice (including safety codes) developed in cooperation with interested industries, professional organizations, and regulatory bodies.

Special Publications—Include proceedings of conferences sponsored by NBS, NBS annual reports, and other special publications appropriate to this grouping such as wall charts, pocket cards, and bibliographies.

Applied Mathematics Series—Mathematical tables, manuals, and studies of special interest to physicists, engineers, chemists, biologists, mathematicians, computer programmers, and others engaged in scientific and technical work.

National Standard Reference Data Series—Provides quantitative data on the physical and chemical properties of materials, compiled from the world's literature and critically evaluated. Developed under a worldwide program coordinated by NBS under the authority of the National Standard Data Act (Public Law 90-396).
NOTE: The Journal of Physical and Chemical Reference Data (JPCRD) is published quarterly for NBS by the American Chemical Society (ACS) and the American Institute of Physics (AIP). Subscriptions, reprints, and supplements are available from ACS, 1155 Sixteenth St., NW, Washington, DC 20056.

Building Science Series—Disseminates technical information developed at the Bureau on building materials, components, systems, and whole structures. The series presents research results, test methods, and performance criteria related to the structural and environmental functions and the durability and safety characteristics of building elements and systems.

Technical Notes—Studies or reports which are complete in themselves but restrictive in their treatment of a subject. Analogous to monographs but not so comprehensive in scope or definitive in treatment of the subject area. Often serve as a vehicle for final reports of work performed at NBS under the sponsorship of other government agencies.

Voluntary Product Standards—Developed under procedures published by the Department of Commerce in Part 10, Title 15, of the Code of Federal Regulations. The standards establish nationally recognized requirements for products, and provide all concerned interests with a basis for common understanding of the characteristics of the products. NBS administers this program as a supplement to the activities of the private sector standardizing organizations.

Consumer Information Series—Practical information, based on NBS research and experience, covering areas of interest to the consumer. Easily understandable language and illustrations provide useful background knowledge for shopping in today's technological marketplace.
Order the **above** *NBS publications from: Superintendent of Documents, Government Printing Office, Washington, DC 20402.*
Order the **following** *NBS publications—FIPS and NBSIR's—from the National Technical Information Service, Springfield, VA 22161.*

Federal Information Processing Standards Publications (FIPS PUB)—Publications in this series collectively constitute the Federal Information Processing Standards Register. The Register serves as the official source of information in the Federal Government regarding standards issued by NBS pursuant to the Federal Property and Administrative Services Act of 1949 as amended, Public Law 89-306 (79 Stat. 1127), and as implemented by Executive Order 11717 (38 FR 12315, dated May 11, 1973) and Part 6 of Title 15 CFR (Code of Federal Regulations).

NBS Interagency Reports (NBSIR)—A special series of interim or final reports on work performed by NBS for outside sponsors (both government and non-government). In general, initial distribution is handled by the sponsor; public distribution is by the National Technical Information Service, Springfield, VA 22161, in paper copy or microfiche form.

U.S. Department of Commerce
National Bureau of Standards
Gaithersburg, MD 20899